Theoret. Comput. Fluid Dynamics (2005) 19: 171–196
Digital Object Identifier (DOI) 10.1007/s00162-004-0108-6

Theoretical and Computational Fluid Dynamics

Original article

A rod-airfoil experiment as benchmark for broadband noise modeling*

Marc C. Jacob[1,2], Jérôme Boudet[1], Damiano Casalino[1,**], Marc Michard[1]

[1] Laboratoire de Mécanique des Fluides et d'Acoustique, Ecole Centrale de Lyon, 36 avenue Guy de Collongue, 69134 Ecully Cedex, France
[2] Université Claude Bernard/Lyon I, 43 boulevard du 11 Nov. 1918, 69622 Villeurbanne Cedex, France

Received July 6, 2003 / Accepted February 11, 2004
Published online July 27, 2004 – © Springer-Verlag 2004
Communicated by P. Sagaut

Abstract. A low Mach number rod-airfoil experiment is shown to be a good benchmark for numerical and theoretical broadband noise modeling. The benchmarking approach is applied to a sound computation from a 2D unsteady-Reynolds-averaged Navier–Stokes (U-RANS) flow field, where 3D effects are partially compensated for by a spanwise statistical model and by a 3D large eddy simulation. The experiment was conducted in the large anechoic wind tunnel of the Ecole Centrale de Lyon. Measurements taken included particle image velocity (PIV) around the airfoil, single hot wire, wall pressure coherence, and far field pressure. These measurements highlight the strong 3D effects responsible for spectral broadening around the rod vortex shedding frequency in the subcritical regime, and the dominance of the noise generated around the airfoil leading edge. The benchmarking approach is illustrated by two examples:

– the validation of a stochastical noise generation model applied to a 2D U-RANS computation;
– the assessment of a 3D LES computation using a new subgrid scale (SGS) model coupled to an advanced-time Ffowcs–Williams and Hawkings sound computation.

In both cases, the ability of computational fluid dynamics to model the source mechanisms and of the CAA approach to predict the far field are assessed separately.

Key words: cylinder-airfoil experiment, broadband noise generation, large eddy simulation, unsteady aerodynamics, subgrid scale model
PACS: 43.28Ra; 47.27Sd; 47.27Eq; 47.85Gj

Correspondence to: M.C. Jacob (e-mail: marc.jacob@ec-lyon.fr)

* The authors wish to thank the European Union for supporting this work under the project TurboNoiseCFD G4RD-CT-1999-00144 coordinated by B.J. Tester, currently visiting Professor at the Institute of Sound and Vibration, Southampton, UK. They also acknowledge Dr. P. Ferrand from CNRS, for providing the computational environment of the related CFD and LES computations.
** *Present address*: Fluorem SAS, 64 chemin des mouilles, 69134 Ecully Cedex, France

1 Introduction

Sound radiation of turbo engines is due to high Reynolds number flows in complex geometries. Two types of noise components can be distinguished.

- The tonal components that are linked to the blade motion periodicity, are deterministic and carry typically half of the sound power in modern ultra high by-pass ratio engines. Although the underlying generation mechanisms are quite well understood, their prediction in the engine design process requires computational fluid dynamics (CFD) tools.
- The broadband part of the noise which carries the other half of the sound power is associated with non periodic and non deterministic flow blade interactions (and with flow self noise in the engine exhaust jet). This component is only partly understood and only some of the source mechanisms are modeled so far. CFD techniques are thus also required for broadband noise prediction, either for fully numerical predictions or as input for analytical models.

In order to directly predict sound sources, and especially broadband sources, highly accurate unsteady CFD solutions must be obtained. This is a major pitfall of turbomachinery sound computations. Indeed, Reynolds-averaged Navier–Stokes (RANS) solvers that are currently applicable and applied to turbomachinery flows, give only orders of magnitudes of the mean flow. They may only give inputs for aeroacoustic models (e.g. wake parameters for rotor/stator interactions). Their recent extension to unsteady aerodynamics is interesting for modeling the deterministic (tonal) sources or quasi-deterministic sources (if stochastic information is provided), as shown hereafter. On the other hand, CFD solvers that are suited for unsteady turbulent flow predictions such as large eddy simulation (LES) or even for complete flow-to-far field simulations (full computational aero acoustics (CAA)), are currently not applicable to turbo engines. The former generally fail to correctly predict the wall flows, whereas the latter are limited both to simple geometries and low Reynolds numbers.

Therefore, extensions of unsteady CFD techniques to the prediction of broadband noise generated by high Reynolds number flows in complex geometries have to be benchmarked on relevant test cases. Such a test case must be based on a geometry that contains some of the aerodynamic mechanisms encountered in turbomachinery applications, but remains simple enough from the computational point of view in order to allow parametric studies. The experiment described in the present paper is designed for this purpose. The configuration is that of an airfoil embedded in the wake of a circular rod. The rod sheds the well-known *von Kármán* vortex street which acts as an oncoming disturbance onto the airfoil.

Flows past rods have been extensively studied since the early work of Strouhal [38] on aeolian tones. A complete review of this topic has recently been published by Zdravkovich [44]. Similarly, unsteady flows past airfoils have been investigated since the mid 1920's [14, 18, 19, 22, 25, 32, 34, 41]. More recently, the latter studies have been generalised [20] and extended to noise predictions by many authors [2, 3, 27, 42] who have set milestones for the prediction of sound radiated by airfoils undergoing sinusoidal perturbations known as gusts. However, although a *von Kármán* street can be regarded as a gust, only very few investigations concerning a rod-airfoil configuration are reported in literature. Stapountzis et al. [37] and Cambanis et al. [10] focused on an airfoil in the near wake (3 rod diameters) of a very large rod (diameter $\sim$ chord) in the context of wind turbines. Other studies that involve splitter plates in the very near wake of a cylinder aim at the control of its vortex shedding (see ref. [1, 39]). Besides this earlier work, ongoing LES computations by Magagnato et al. [26] and Sorguven et al. [36] are compared for the reference configuration of the present investigation and also compared to some of its experimental results.

For the following reasons, the rod-airfoil configuration is a relevant test case for broadband noise modeling:

- At high Reynolds numbers, the rod wake combines the periodic vortex shedding with a random perturbation due to the wake's transition into turbulence [44].
- As a result, the airfoil undergoes a broadband perturbation that is dominated by a preferred shedding frequency, somewhat like that observed in turbomachinery applications.
- The ability of a combined CFD/acoustic approach to predict the spectral broadening around the shedding frequency and its harmonics is a relevant measure of its ability to model broadband sources.

– Besides these general features, the test case also involves several important noise generation mechanisms encountered in aeroengines (ingestion of turbulence by a fan, and rotor-stator interactions).
– The experiment gives clear results. The quantities of interest are not affected by installation effects as discussed in this paper. In particular, spectral broadening due to the rod-airfoil configuration outranges other broadband sources (jet noise etc.).

This benchmark can be applied to various unsteady CFD techniques associated with acoustic models. In the case of U-RANS that predicts only the deterministic part of the flow, it allows testing of the aeroacoutsic model. In the case of LES, which is able to predict the lower end of the turbulence spectrum, it allows testing of the applicability of the code to complex wall flows. In particular, the robustness of the subgrid scale (SGS) model at the wall can thus be tested.

The experimental procedure is described in Sect. 2, and results are given in Sects. 3 to 5. The mean flow and the statistics of the fluctuating flow are discussed in Sect. 3, whereas instantaneous flow features are shown in Sect. 4. Section 5 is devoted to the acoustic far field.

The benchmarking approach is illustrated in Sect. 6 by two examples:

– a 2D unsteady RANS (U-RANS) computation combined with an acoustic model based on the Ffwocs–Williams–Hawkings equation and on a stochastic modeling of the spanwise pressure distribution;
– a 3D LES using a new SGS model whose instantaneous fields are fed into an advanced time formulation of the Ffowcs–Williams and Hawkings analogy for arbitrary integration surfaces.

Not only are the aerodynamic and acoustic statistics compared to experimental data, but also the instantaneous flow fields.

2 Experimental set-up and measurement techniques

2.1 Flow configuration

The experiment was conducted in the large anechoic room of the ECL (10 m × 8 m × 8 m). Air was supplied by a high-speed subsonic anechoic wind tunnel at Mach numbers ranging up to 0.34.

The experimental set-up and the co-ordinates are shown in Fig. 1. The reference configuration is that of a symmetric NACA-0012 airfoil (chord: $c = 100$ mm; thickness: $e = 12$ mm) located one chord downstream of a rod ($d/c = 0.1$), both extending by $l = 300$ mm in the spanwise direction. In the reference configuration, the airfoil chord is nearly aligned with the center of the rod cross-section. Due to wood manufacturing of the end plates, there is a $y = -2$ mm shift between the rod axis and the airfoil chord. As a result the mean flow is parallel to the chord but the cylinder wake is slightly shifted into the $y > 0$ direction with respect to the chord. Since the rod wake mean velocity is varying in y, this shift results in a slight angle of attack of 2° as found recently by Boudet [8]. This has some impact on the airfoil wake symmetry and on the airfoil mean pressure distribution but does not affect the leading edge interaction mechanism. The airfoil-rod distance is sufficient to avoid significant feedback of the airfoil onto the shedding. The set of two bodies is placed in the potential core of a free rectangular jet. This jet is partially flanged by the two wooden end plates that contain the supports of the two bodies. The rod and the airfoil supports are concentric disks, allowing for the rod and the airfoil to be rotated independently around a common axis. Hence non-symmetric configurations with high angles of attack can be investigated. The lower inner disk supporting the airfoil is a glass window for laser PIV measurements whereas all of the other disks are wooden. One other rod ($d/c = 0.16$) is also examined. The measurements are carried out at several incoming velocities ranging from $U_0 = 30.5\,\mathrm{m\,s^{-1}}$ to $U_0 = 117\,\mathrm{m^{-1}}$. Unless otherwise specified, all results presented in this paper are obtained in the reference configuration at $U_0 = 72\,\mathrm{m\,s^{-1}}$. The atmospheric pressure was 98.9 kPa. The ambient temperature was 293 ± 2 K; however, during hotwire measurements, much higher temperatures and temperature variations (298 ± 5 K) occurred due to daily fluctuations. Suitable corrections have been made to the hotwire data to express them at 293 K. Comparisons between experiment and CFD can thus be made at 293 K.

Under these conditions, the rod diameter based Reynolds number Re_d is about 48 000 in the reference configuration, and the corresponding Mach number $M_0 \sim 0.2$, gives a shedding frequency f_0 in the rod wake of about 1.3 kHz, which corresponds to a Strouhal number $St_0 = f_0 d/U_0 = 0.19$. The various configurations are summarized on Table 1.

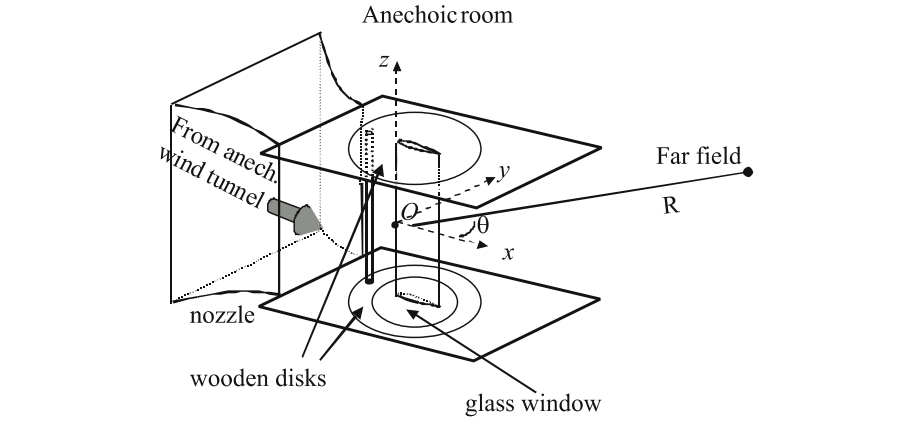

3D view

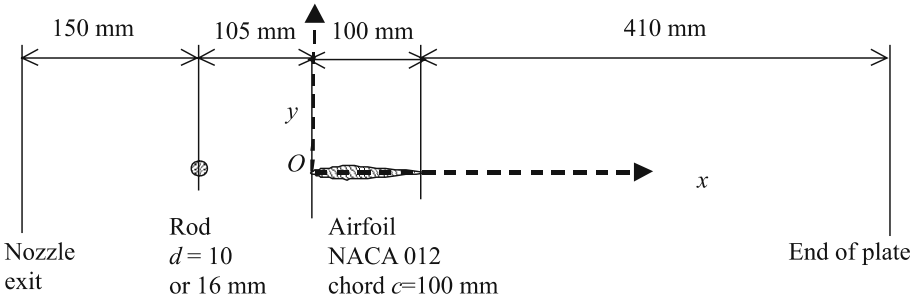

top view

Fig. 1. Sketch of the experimental set-up, top: 3D view; bottom: top view

Table 1. Summary of different configurations and operating conditions

d	0.01 m				0.016 m			
U_0	30.5	61	72	115	30.5	61	72	117
Re_d	20 400	40 700	48 000	78 000	32 600	65 100	76 800	125 000
Re_c	204 000	407 000	480 000	780 000	204 000	407 000	480 000	780 000
M	0.09	0.18	0.21	0.34	0.09	0.18	0.21	0.34

2.2 Aerodynamic measurements

The velocity field is investigated in the mid-span plane ($z = 0$).

2.2.1 Particle image velocity (PIV)

Particle image velocimetry (PIV) measurements are carried out in the vicinity of the airfoil but not near the rod in order to obtain more flow details as well as snapshots of the flow field in that region. A classical commercial Dantec PIV system described by Bera et al. [4] is used. A laser sheet is obtained on the measurement plane and a video camera is placed beneath the glass disk, its axis being normal to the sheet. Seeding is carried out far upstream near the fan in order to obtain a homogeneous particle distribution in the measurement plane. Five areas of interest are investigated in the vicinity of the airfoil (cf. Fig. 2), with different magnification factors. Plane (a) is meant to characterise the disturbance coming onto the airfoil from the rod. It extends roughly from half a chord upstream, down to the first quarter chord of the

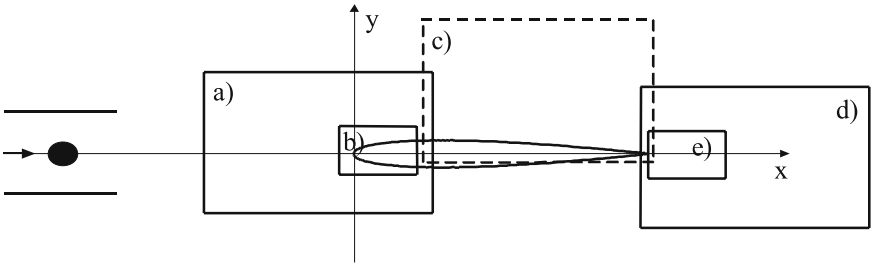

Fig. 2. Location of PIV measurement planes

airfoil. Plane (b) is a zoom on the airfoil leading edge that gives a more precise insight of the flow distortion near the leading edge. Plane (c) provides a view of the flow along the slender part of the airfoil. Planes (d) and (e) focus on the wake and the near wake of the airfoil respectively. A triangle is missing in planes (a), (b), (d), and (e) corresponding to the shadow zone of the laser sheet. The dimensions of planes (a), (c), and (d) are $78.1 \times 62.5\,\mathrm{mm}^2$, whereas the zoom planes (b) and (e) are $25 \times 21\,\mathrm{mm}^2$ wide. The velocity fields are obtained with a graphic resolution of 32×32 pixels. Hence, the spatial resolution of the PIV measurements ($0.75 \times 0.75\,\mathrm{mm}^2$ for planes (a), (c), and (d), and $0.5 \times 0.5\,\mathrm{mm}^2$ for the zooms) is not sufficient to capture the structure of the boundary layer developing along the airfoil wall. The PIV time resolution is limited by the characteristics of both the laser system and the camera. In the present case it is about 4.5 Hz. Thus the consecutive snapshots of the flow field are not co-related to each other in the present study since the shedding frequency is about 1.3 kHz. Post-processing details are given in Sect. 2.3.

2.2.2 Hot wire

In order to complete the PIV information, a few single hot-wire measurements are carried out in the reference configuration at $U_0 = 72\,\mathrm{m\,s}^{-1}$ ($M_0 \sim 0.2$). They provide the mean velocity magnitude and if the turbulence is not to high, the velocity fluctuations (level and spectra), in the local mean flow direction at various cross-sections. In particular, they give the upstream conditions at the nozzle outlet, which are important for benchmarking purposes, global characteristics of the flow near the rod and airfoil far wake information. Measurements are carried out with an IFA 100 Anemometer.

2.2.3 Wall pressure coherence

The wall pressure coherence is measured with a set of pressure probes in order to study the chordwise coherence near the mid-span of the airfoil and the spanwise coherence distributions along the rod. These probes are remote microphone probes using Electret microphones described elsewhere [31]. Measurements are performed at various flow speeds with the two rods. Coherence between the aerodynamic and the acoustic fields at an observation angle of $-90°$ (microphone facing the probes) is measured. Data acquisition is performed with a spectral resolution of 4 Hz and the number of averages is 500.

2.3 Processing of the PIV and the hotwire data

2.3.1 Classical flow field statistics

Flow statistics are computed at each location of the flow by ensemble averaging over a set of 500 instantaneous velocity fields (or snapshots):

- U and V are the ensemble-average mean velocity components of the velocity $\mathbf{U}$ in the x and y directions respectively; U_{mean} is the modulus of the mean velocity that can be derived from a single hot-wire's mean voltage.
- u' and v' are the root-mean-square (*rms*) values of the corresponding velocity fluctuations, u and v; u_{rms} is the *rms* value of the velocity fluctuations in the local mean flow direction that can be derived from a single hotwire's *rms* voltage.
- $\mathcal{R}_{uu}\left(\mathbf{x}, \mathbf{x}'\right)$ and $\mathcal{R}_{vv}\left(\mathbf{x}, \mathbf{x}'\right)$ are the normalised spatial co–relation coefficients of u and v respectively, computed at a given location $\mathbf{x}$, for every location $\mathbf{x}'$ in the flow.

2.3.2 Identification of vortical structures

Vortical structures are identified with two dimensionless scalar functions $\Gamma_1(x)$ and $\Gamma_2(x)$ following the work of Michard et al. [28] and Graftieaux et al. [21]. These functions are based on the normal angular momentum (NAM) that is derived from the measured velocity field. They are related to the topology of streamlines around a current position x in a local convected frame and are bounded between -1 and 1. They give the locus of a vortex center and the region of its solid body core. For each vortex, Γ_1 is a spatial pulse whose peak value is the sign of vorticity (-1 or 1) at the vortex center and decays very quickly away from the center. Γ_2 is like a windowing function. Its values are neighbouring the vorticity sign (1 or -1) in the region where the rotation rate outranges the strain rate. This function allows separation of the regions of dominant rotation rate from the regions of dominant strain rate. The separation occurs for $|\Gamma_2| = 2/\pi$. Hence this function points out the shape of a vortex independently from its strength.

2.3.3 Proper orthogonal decomposition (POD) analysis

A POD analysis of the unsteady velocity field is performed by computing a modal basis from a set of 500 snapshots as described in ref. [21] and ref. [29]. Each fluctuating velocity field is projected on the modal basis. The unsteady character of the flow is included in the coefficients of the decomposition. The objective of the POD analysis is to emphasise the dynamical significance of a small number of modes (the first modes if the corresponding eigenvalues are sorted from the largest to the smallest) containing the main features of the incoming unsteady and spatially periodic disturbances.

2.4 Acoustic far field

Acoustic measurements are conducted in the far field at a distance $R = 1.85$ m from the airfoil center (half chord, downstream of the leading edge), in the mid-pan plane ($z = 0$, see Fig. 1). Two Brüel & Kjäer type 4191 microphones with Brüel & Kjäer type 2669 preamplifiers are used for these measurements and are rotated around the center of the airfoil.

The directivity of the sound pressure level as well as spectra are measured for various flow configurations. For simplicity, only the velocity dependence in the reference configuration is presented in this article. The rod-alone configuration and the "background noise" (no airfoil or rod) are also measured in order to check the contribution of the airfoil in the rod-airfoil configuration. Data acquisition is carried out with a spectral resolution of 4 Hz and the number of averages is 200.

3 Aerodynamic results

3.1 Mean flow and one point fluctuations statistics

The main results of the hot wire anemometry are summarised in Figs. 3 and 4, while the mean flow velocity and *rms* fluctuations from the PIV are illustrated on Fig. 5. The hot wire profiles are shown in typical cross-sections to characterise the incoming flow (i), the rod near wake (ii), the flow along the airfoil (iii), and the airfoil far wake (iv). Figure 3 is divided into four plots. Each plot shows the profiles of the mean velocity modulus U_{mean} (top subplot) and of the corresponding *rms* velocity fluctuations u_{rms} in the local mean flow direction (bottom subplot). The velocities are made non-dimensional by U_0 and the co-ordinates are scaled against the airfoil chord. Figure 4 is divided into four plots corresponding to the same cross-sections as in Fig. 3. It shows the velocity spectra at different locations, with each plot gathering points for a given cross-section. The spectra are plotted in dB, with a $1\ \text{m}^2\ \text{s}^{-2}$ reference versus the Strouhal number based on the rod diameter d and the flow speed U_0. The y co-ordinates are expressed in terms of d since the peaks are due to the rod vortex shedding. Figure 5 shows PIV velocity charts around the leading edge. It is divided into 6 plots. U, V, u', and v' are represented in plot (i), (ii), (iii), and (iv) respectively, and cover the PIV plane (a). details of u' and v' (PIV plane b)) are shown in plots (v) and (vi), respectively. Results from other regions are not shown in this paper. Co-ordinates are scaled against the chord c, and velocities against U_0. Figures 3 and

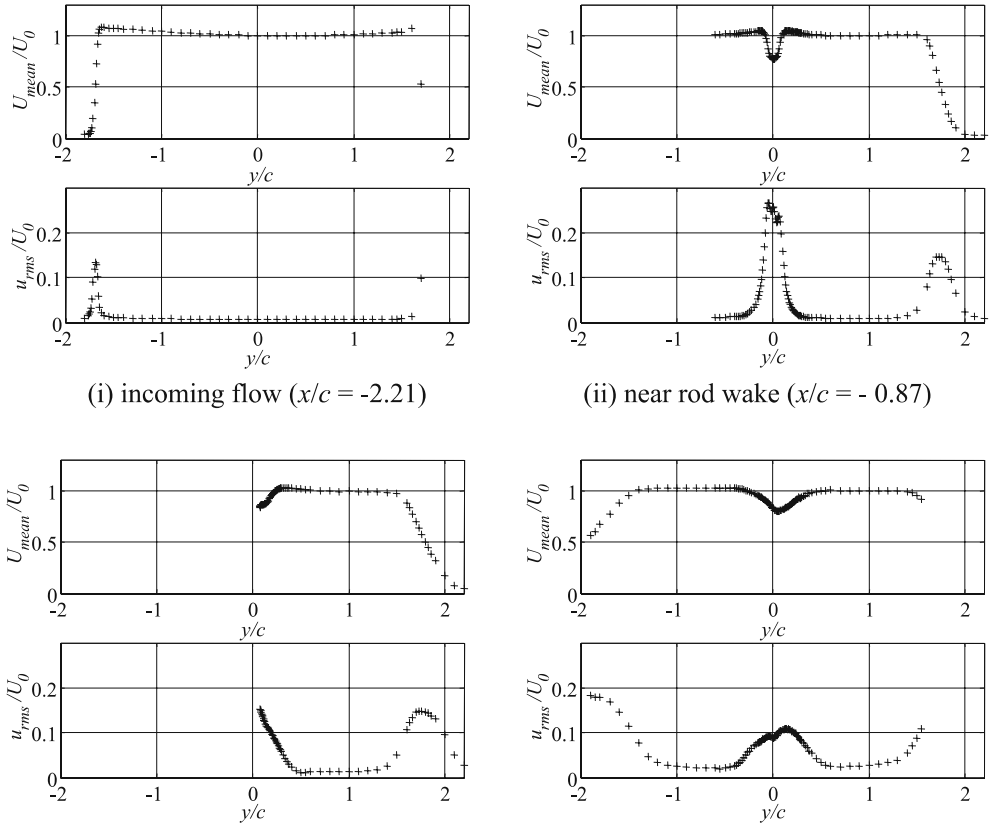

Fig. 3. Profiles of mean flow velocity and *rms* values of turbulent fluctuations in the mean flow direction obtained by hot wire anemometry at various cross-sections. Plot (i): incoming flow; plot (ii): near rod wake; plot (iii): aside airfoil; plot (iv): far airfoil wake, top subplot: U_{mean}/U_0 versus y/c; bottom subplot: u_{rms}/U_0 versus y/c

4 confirm that the rod-airfoil set-up is indeed in the potential core of the jet. At one chord downstream of the airfoil trailing edge, the core is still 2 chords wide, that is, about 2/3 of its size at the nozzle exit.

The incoming flow (at the nozzle outlet) has a top-hat profile and the turbulence level remains small ($u_{rms}/U_{\text{mean}} \approx 0.78\%$) in the central part, away from the jet shear layers (Fig. 3 – plot (i)). In Fig. 4 – plot (i), the peak at $St_0 = 0.19 \pm 0.002$ corresponds to the rod shedding frequency and is due to sound waves propagating upstream away from the rod. It is detected because of the low turbulence level. It is not detectable in the highly turbulent jet shear layers (plot 4(i) – $y/d = 16.9$).

The near wake velocity deficit and the increase in velocity fluctuations that appear downstream of the rod, are shown on Fig. 3 plot (ii). The two initial rod shear layers (each containing vortices shed at one side) can still be guessed from this plot. Further downstream, the shear layers merge and the wake spreads as it approaches the airfoil where it extends over a fairly wide region (Fig. 5 plot (i)). It reaches about $8d$, that is, 0.8 chord at $x = -0.25c$. The fluctuations are mainly due to the shed vortices as shown on Fig. 4 plot (ii). Plots (iii) and (iv) of Fig. 5 shows that upstream of the leading edge v' is much larger than u'. This results from the vortex street pattern. The shedding Strouhal number is about 0.19. It should be noted however, that this value corresponds to the maximum value of the peak which appears to spread over a large range of frequencies. Near the rod, the velocity fluctuations away from the $y = 0$ axis are mainly due to the vortices shed by one side of the rod. Therefore the corresponding spectra mainly contain the fundamental frequency and uneven harmonics, whereas the spectrum on the rod axis is dominated by even harmonics. This can be explained by the fact that on the x-axis, the flow is equally influenced by the vortices shed from both sides of the rod, and the contribution to streamwise fluctuations has the same sign.

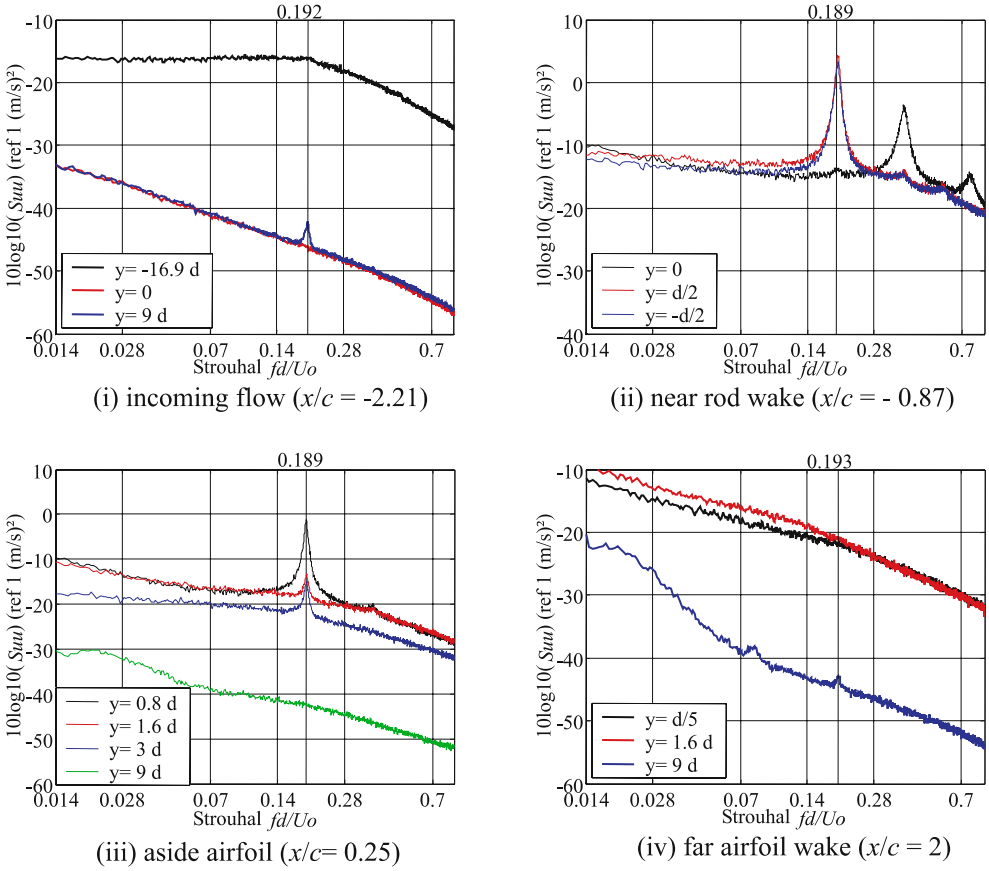

Fig. 4. Velocity spectra S_{uu} in dB versus Strouhal number $St = fd/U_0$ at different locations. Plot (i): incoming flow; plot (ii): near rod wake; plot (iii): aside airfoil; plot (iv): far airfoil wake

Along the airfoil, the mean flow is still strongly influenced by the rod wake, with the effect of the airfoil resulting in an acceleration which partly compensates the deficit due to the rod wake (Fig. 3 plot (iii)). Plots (i) and (ii) of Fig. 5, where both velocity components are plotted separately, clearly shows the rise of the V component along with a reduction of the U component near the leading edge. Moreover, the zooms on plots (v) and (vi) of Fig. 5 show how the velocity fluctuations are affected by the leading edge. Hence u' vanishes and its energy is transferred into the v' component. The spectra in plot (iii) of Fig. 4 show that the vortices shed by the rod still dominate the fluctuating velocity field in that region. The first harmonic of the shedding frequency is detectable near the leading edge. This might be due to the fact that some vorticity from one side of the rod is convected past the opposite side of the airfoil. It might also be due to the fact that the oncoming streamwise fluctuations near the x axis, which contribute to the pressure fluctuations in the leading edge region, also contain the even harmonics of the shedding frequency. The PIV snapshots give another view of that particular aspect (see Sect. 4).

In the far wake of the airfoil, the flow returns to a broadband wake as shown in the corresponding spectra (Fig. 4 plot (iv)). The peak due to the rod vortices is only detectable outside the wake ($y = 9d$) where the flow is quiet, for the same reasons as it was detectable at the nozzle outlet. The wake is slightly asymmetric (Fig. 3 plot (iv)). This is due to the 2° angle of attack and to the fact that rod is not perfectly centered on the x axis (a $y = -2$ mm shift has been measured). This shift can also be inferred from the rod wake fluctuations (Fig. 3 – plot (ii)).

3.2 Two-point velocity co–relations

One way to statistically characterise the turbulence around the airfoil is to analyse spatial two-point co–relations. Thus, the spatially coherent part of the fluctuating flow is emphasised. A few examples are shown

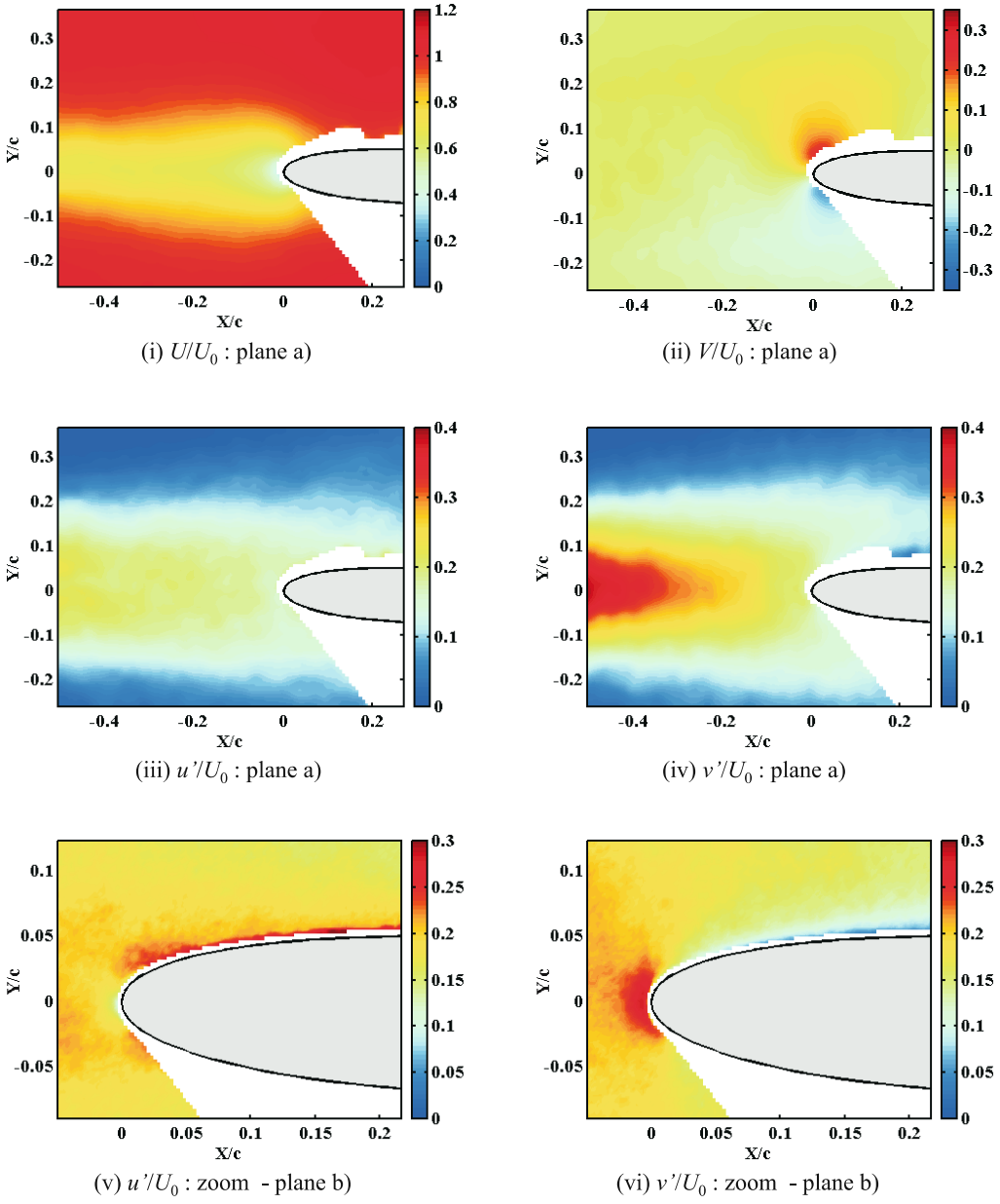

Fig. 5. Examples of mean flow velocity and *rms* values of turbulent fluctuation components obtained from PIV near the leading edge

in Fig. 6. The spatial co–relation coefficients $\mathcal{R}_{uu}(\mathbf{x}, \mathbf{x}')$ and $\mathcal{R}_{vv}(\mathbf{x}, \mathbf{x}')$ are plotted versus $\mathbf{x}'$ in planes (a), (c), and (e) for 1 and 2 $\mathbf{x}$ locations respectively.

The top plots of Fig. 6 are obtained for $\mathbf{x}(-0.05c, 0)$, which is a location near the leading edge. It can be seen that $\mathcal{R}_{vv}$ is very high in the rod wake (with values oscillating between -1 and 1) and is spatially periodic, whereas $\mathcal{R}_{uu}$ is much weaker. This is due to the larger values of v' compared to u', as mentioned in Sect. 3.1. The plots also suggest that the fluctuation level found at the leading edge is a remainder of the rod flow perturbation since the flow co–relation is close to 1 between two vortices shed by the same side and close to -1 between vortices shed from opposite sides. The mean distance between two vortices can be estimated as 21 mm ($\sim 0.2c$), that is a distance of 42 mm ($\sim 0.4c$) between two vortices shed at the same side of the cylinder.

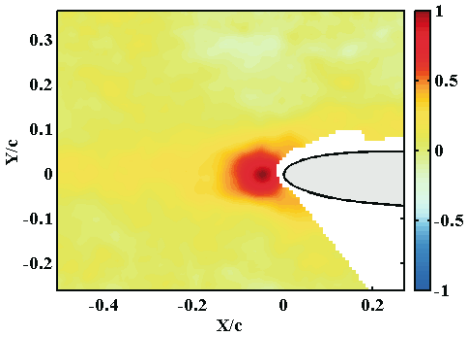

(i) $\Re_{uu}$ (x/c= -0.05; y/c= 0): plane a)

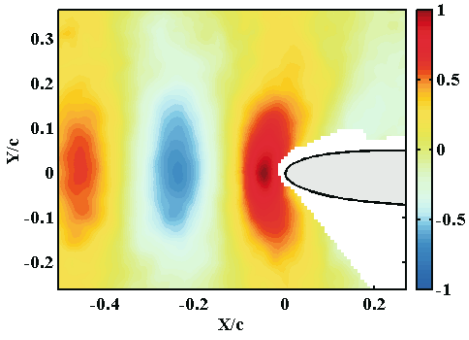

(ii) $\Re_{vv}$ (x/c= -0.05; y/c= 0): plane a)

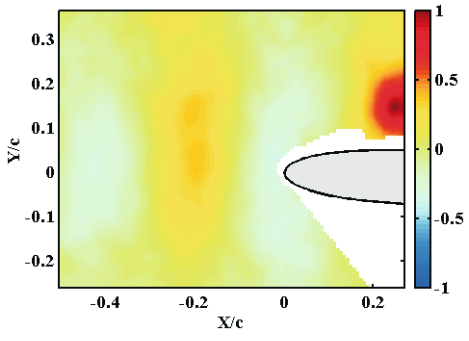

(iii) $\Re_{vv}$ (x/c = 0.25 ; y/c = 0.15): plane a)

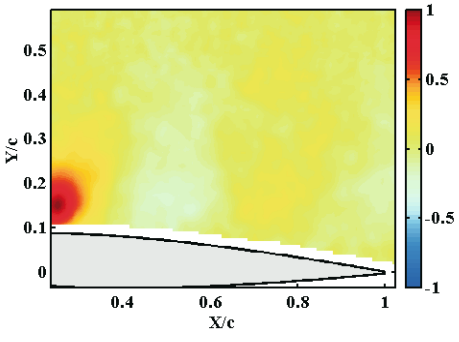

(iv) $\Re_{vv}$ (x/c = 0.25 ; y/c = 0.15): plane c)

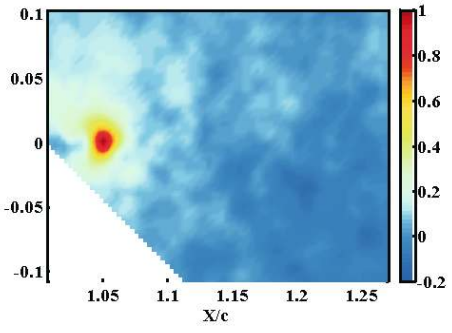

(v) $\Re_{vv}$ (x/c = 1.05 ; y/c = 0): plane e)

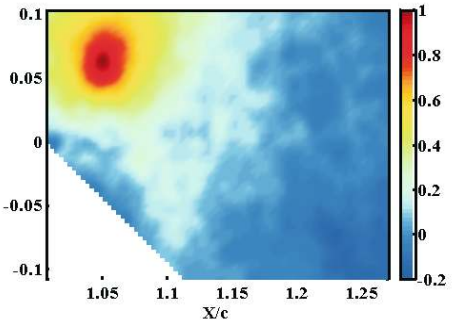

(vi) $\Re_{vv}$ (x/c = 1.05 ; ,y/c = 0.06): plane e)

Fig. 6. Spatial velocity co-relation coefficient. Plot (i): $\mathcal{R}_{uu}$ at $(x/c, y/c) = (-0.05, 0)$. Other plots: $\mathcal{R}_{vv}$ for various co-relation points. Plot (ii): $(x/c, y/c) = (-0.05, 0)$; plots (iii) and (iv): $(x/c, y/c) = (0.25, 0.15)$; plot (v): $(x/c, y/c) = (1.05, 0.06)$

Plots (iii) and (iv) in Fig. 6 are obtained for x located $0.25c$ downstream of the leading edge at $y/c = 0.15$. Only $\mathcal{R}_{vv}(\mathbf{x}, \mathbf{x}')$ is plotted. Plot (iii) shows the upstream co–relation for this point (PIV plane a)) whereas the downstream co–relations (PIV plane c)) are shown in plot (iv). A comparison between these plots and plot (ii) shows that the flow is much more weakly co–related to the *von Kármán* street as x is moved downstream. Moreover, at a given co–relation point $\mathbf{x}$, the downstream co–relation is much weaker than the upstream co–relation. These observations suggest that the part of the fluctuating flow due to the rod disturbances is reduced because the vortices are distorted as turbulence develops. Thus, the rod disturbances loose some spatial coherence. Note that a positive co–relation with the other side of the airfoil can be guessed from the center plots of Fig. 6. The v co–relation near the trailing edge is shown on the bottom plots (v) and (vi) of Fig. 6 for two points $\mathbf{x}$ $(1.05c, 0)$ and $\mathbf{x}$ $(1.05c, 0.06c)$ respectively. The co–relation size is clearly larger in the second case suggesting that

the flow is carrying mainly two types of eddies, as shown by the remainders of the large rod vortices that are swept past the airfoil in plot (vi), and by the new eddies generated at the airfoil trailing edge in plot (v).

3.3 Wall pressure coherence

3.3.1 Incoming disturbance

The acoustic efficiency of the vortex shedding is strongly dependent on its spanwise coherence, as discussed for the case of an isolated rod [13] and in the case of a rod-airfoil configuration [11]. As shown in Fig. 7 the spanwise coherence along the cross-stream facing side decays exponentially with η^2 (η being the spanwise separation) for the two rods. This Gaussian decay is indicated by the best fit curves that are plotted for various flow velocities in Fig. 7. The Gaussian coherence length Lg is between five and six rod diameters for most cases. The highest value ($7d$) is obtained at $72\,\mathrm{m\,s^{-1}}$ for the $d = 0.01$ rod. For the $d = 16\,\mathrm{mm}$ rod it seems to decrease slowly with increasing flow speed.

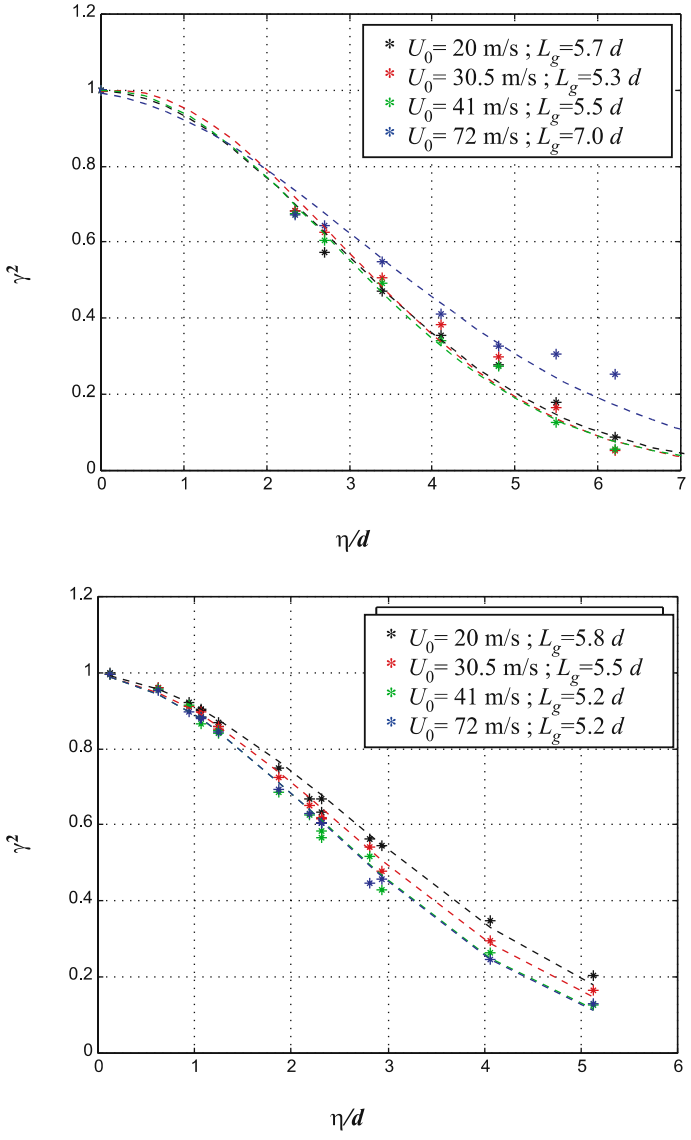

Fig. 7. Spanwise coherence γ^2 of the rod pressure field at the shedding frequency against η/d, the non dimensional spanwise distance separation between the two co-relation points. Top: $d = 0.01\,\mathrm{m}$ rod; bottom: $d = 0.016\,\mathrm{m}$ rod. Symbols are the measured values; the continuous lines are the Gaussian interpolation

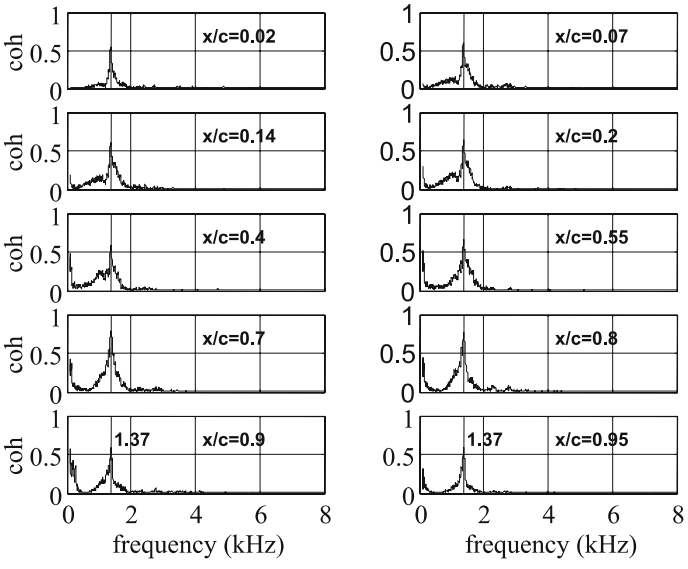

Fig. 8. Coherence between the airfoil and the far field at $U_0 = 72\,\mathrm{m/s}$, increasing x/c from left to right and from top to bottom

3.3.2 Coherence between airfoil wall pressure and far field

Coherence between the wall pressure field on the airfoil and the acoustic far field at an observation angle of $-90°$ is shown in Fig. 8 for the reference configuration. The probe location varies from $x/c = 0.2$ to 0.95. A strong coherence is found for a broad range of frequencies around the main peak all over the airfoil. In the low frequency range, increasing coherence levels are found on the slender part of the airfoil. They are probably due to the deformation of the rod vortices interacting with the surrounding turbulence. Note that the coherence between a flow probe and the far field only proves that the local fluctuation is related to a source but does not indicate where the actual source is located. Chord-wise coherence measurements not shown here, confirm that the rod disturbances remain coherent past the airfoil, although their intensity decreases towards the trailing edge, and the accompanying pressure signals show that the strongest pressure levels are found near the leading edge.

4 The instantaneous flow field

4.1 Interpretation of instantaneous velocity fields

Only a few examples of snapshots can be shown in this paper. Figure 9 shows the results of various post-processing techniques described in Sect. 2.3 for a typical snapshot in plane (a) in the reference configuration. All plots are obtained from the same snapshot obtained in the reference configuration. The fluctuating velocity field and its corresponding vorticity map are given respectively in plots (i) and (ii). These maps show that the velocity field consists of a small scale turbulent field embedded in larger *von Kármán* vortices shed by the rod. The small-scale turbulence accounts for a high spatial intermittency. As a result, the location and geometry of the large vortices can almost not be determined.

In order to highlight major vortical structures, various post-processing techniques are applied. Plots (iii) and (iv) of Fig. 9 show the main vortex center locations and sizes obtained from the velocity field using Γ_1 and Γ_2. The large rod vortices are clearly distinguishable. If the POD analysis is applied, the first three to four modes appear to dominate the flow dynamics. Mode 0 corresponds to the mean flow and modes 1 and 2 contribute up to nearly 40% of the velocity fluctuation energy. It has been shown [29], that these modes can be interpreted as a periodic streamwise array of staggered large vortices, whose wavelength, far upstream of the airfoil, is consistent with the value determined in Sect. 3.2 from the two-point velocity co–relation coefficient. Michard et al. [29] also showed that the vortex-airfoil interaction is quite satisfactorily described by these modes (splitting at the leading edge, stretching along the airfoil). Hence, the 3 first

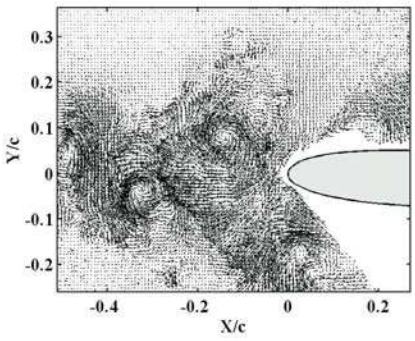

(i) instantaneous relative velocity field

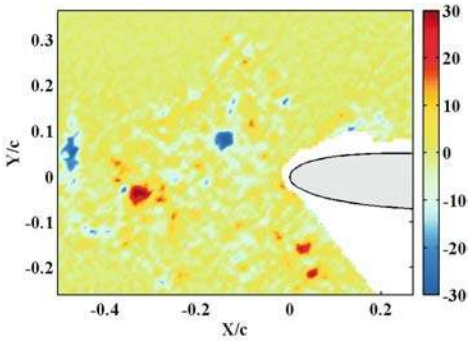

(ii) corresponding vorticity

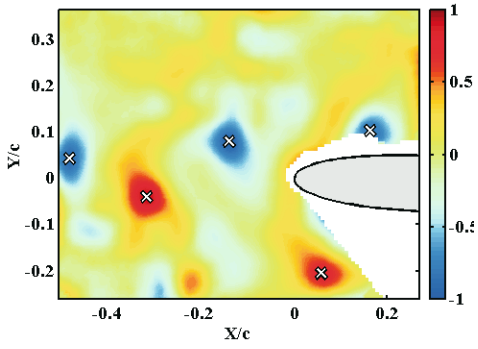

(iii) vortex centre location(adapted from Γ_2)

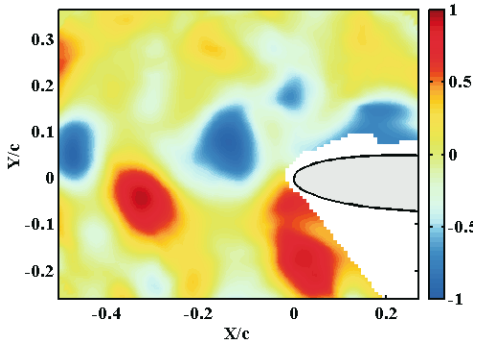

(iv) vortex extent (Γ_2 function)

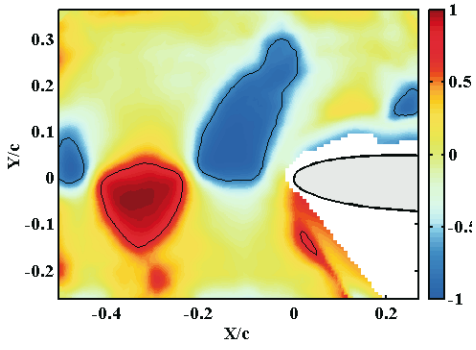

(v) vortex extent (Γ_2 function) : reconstructed from 3 first POD modes

Fig. 9. Various interpretations of the same snapshot obtained in the reference configuration in region (a). Plot (i): instantaneous relative velocity field; plot (ii): corresponding spanwise vorticity; plot (iii): vortex center locations (Γ_1 adapted from Γ_2); plot (iv): vortex extent (Γ_2 function or NAM) plot (v): vortex extent (Γ_2 function) reconstructed from the 3 first POD modes

modes are essential in the rod-airfoil interaction process. In plot (v) of Fig. 9, Γ_2 is applied to the instantaneous flow field reconstructed with the 3 first modes (the black lines correspond to the core contours). The large-scale instantaneous features highlighted in plot (iv) are quite well featured. More POD results are detailed elsewhere [7].

This example shows that both POD and the Γ_2 function appear to be efficient tools for identifying and describing the large scale characteristics of the incoming vortices, and their subsequent evolution along the airfoil.

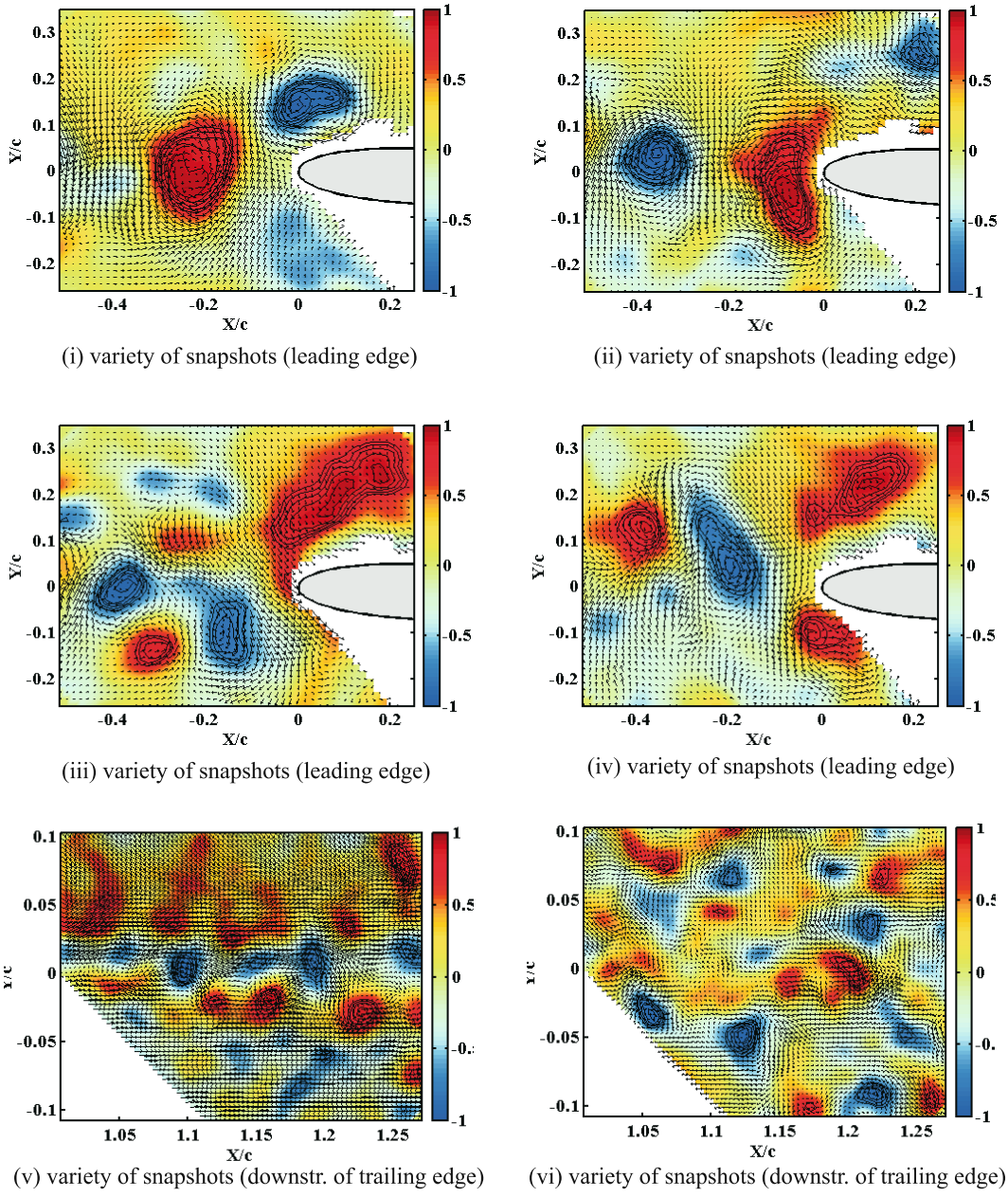

(i) variety of snapshots (leading edge)

(ii) variety of snapshots (leading edge)

(iii) variety of snapshots (leading edge)

(iv) variety of snapshots (leading edge)

(v) variety of snapshots (downstr. of trailing edge)

(vi) variety of snapshots (downstr. of trailing edge)

Fig. 10. Relative velocity vectors and Γ_2 (NAM) for various upstream of the leading edge (top) and downstream of the trailing edge (bottom) illustrating the variety and complexity of the instantaneous flow

4.2 Variety of instantaneous flow patterns

In order to illustrate the complexity and the intermittency of the fluctuating flow, six snapshots are plotted in Fig. 10. The vectors and the colours represent the velocity fluctuations and the Γ_2 function respectively. The contours indicate iso-values of Γ_2 (the outmost contour of a vortex is the core limit).

In plots (i) to (iv), four snapshots of the unsteady flow around the leading edge are shown. The following conclusions can be drawn from these typical snapshots.

– In the leading edge region, the vortices undergo strong deformation.
– Some incoming vortices that are almost located on the $y = 0$ axis, impact on the leading edge and are split into two parts.

– Others are already split before reaching the stagnation point.
– Most vortices shed by a given side of the rod are convected past the same side of the airfoil.
– However, some vortices pass along the opposite side of the airfoil (a $y > 0$ vortex might switch to $y < 0$ and vice versa).
– Beside the main vortices, smaller ones appear despite the Γ_2 filter. This illustrates the complexity of the large-scale structure dynamics in the leading edge region.

On these instantaneous fields, the distance between two (opposite) vortices is also found to be about 21 mm ($\sim 0.2c$) when the vortices can be well recognised. In plots (v) and (vi) of Fig. 10, the same quantities are plotted in the airfoil wake region (plane d). Again, the complexity of the snapshots is striking. In the bottom left plot, the nascent airfoil wake can be recognised, whereas it is hardly distinguishable in the bottom right plot. The rod vortices can still be guessed but appear much less spatially organised near the leading edge. This is in agreement with hot wire spectra (Sect. 3.1) and spatial co–relation measurements (Sect. 3.2). The present results highlight the complexity of the instantaneous flow and show the key role of the leading edge in the evolution of the incoming rod perturbation. In particular, the strong vortex airfoil interaction suggests that the leading edge is the main source region in this flow configuration.

5 Acoustic results

5.1 Spectra

A typical set of spectra is shown in Fig. 11 for the reference configuration. The spectra of the noise generated by the flow only, the $d = 10$ mm isolated rod, and the complete configuration are plotted. The microphone is at 90° to the flow direction and the power spectrum density is plotted in dB versus the Strouhal number.

Several conclusions can be drawn from this figure.

– First of all, the flow noise is significantly increased over a wide range of frequencies for the two configurations with a rod. This shows that the vortex shedding is not merely responsible for a tonal sound radiation. The spectrum is broadened around the main peak and this phenomenon is enhanced by the airfoil.
– Secondly, the broadband part of the spectrum clearly outranges the background noise (jet noise etc.) in the frequency range of interest. Thus, the spectral broadening is due to the flow interacting with the rod-airfoil system; since in the very low frequency range, all the spectra merge, it can be inferred that the rod-airfoil system has no significant influence onto the installation effects (like jet deflection, feedback to nozzle outlet and so on). As mentioned in the introduction, this is an important criterion in selecting this configuration as a benchmark.

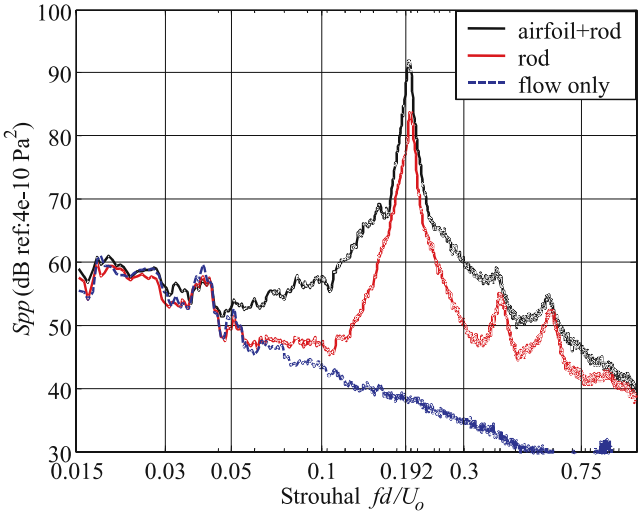

Fig. 11. Power Spectral density against $St = fd/U_0$, far field spectra normal to the flow direction (90°). Upper black curve: rod + airfoil; red: rod only; lower black curve: flow only

– Thirdly, the level is about 10 dB higher when the airfoil is embedded in the flow, thus the overall sound level is dominated by the airfoil, at least at this observation angle.

The Strouhal number of the main peak is somewhat higher without the airfoil, it is 0.195 in the rod-only configuration instead of 0.192. The corresponding 20 Hz shift is physical since the spectral resolution is $\Delta f = 4$ Hz. This might be due to a slight modification of the vortex shedding by its interaction with the airfoil suggesting a weak feedback of the airfoil onto the rod.

5.2 *Sound levels*

The far field directivity of the main peak is plotted in Fig. 12 for flow velocities ranging from 30.5 m s^{-1} to 117 m s^{-1}. The SPL which is given in dB (ref. 2×10^{-5} Pa) decreases away from 90° faster than it does for a corresponding point dipole (not represented here). Since the Mach number reaches about 0.3 for the 117 m s^{-1} case, refraction by the jet shear layers is not negligible. Therefore the corrected directivity (i.e. when these effects are removed) is also plotted for each case *via* an angular correction, $\cos\theta_2 = \cos\theta_1 / (1 - M_0 \cos\theta_1)$, where $\cos\theta_1$ is the refracted angle (in the present case it is a good approximation of the observation angle θ), $\cos\theta_2$ is the actual emission angle, and M_0 is the flow Mach number. The far field measurements also show that the sound pressure level of the main peak varies with the 5.2th power of the flow velocity. This result proves that the airfoil does not behave as a compact dipole since this would lead to a U_0^6 power law. In fact such power laws characterise diffraction of turbulent eddies by edges [17]. This suggests that the dominant sound source is located at one of the airfoils edges, and is in fact the leading edge as shown by the PIV study.

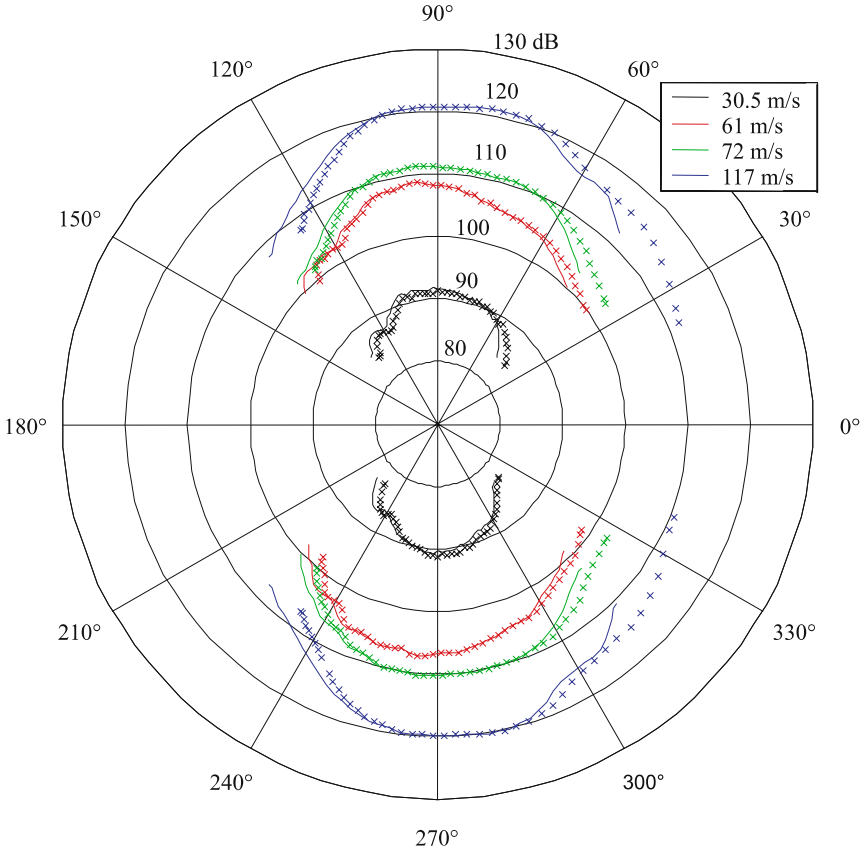

Fig. 12. Directional pattern of the main Strouhal peak at various flow speeds. Mean flow effects on propagation: line (—): uncorrected; symbols (× × ×): corrected, each colour stands for a velocity

6 Two examples of benchmarking

This section illustrates how unsteady CFD calculations associated with appropriate acoustic models can be tested against the data described above and how their ability to model broadband noise can be assessed. An example is given for two popular CFD approaches, unsteady Reynolds-averaged Navier–Stokes (U-RANS) and large eddy simulation (LES). All results discussed hereafter are obtained in the reference configuration for a zero degree angle of attack.

6.1 Numerical approach

6.1.1 Flow solver

The finite volume compressible U-RANS code *Proust* is used in the current investigation [5]. The convective and diffusive fluxes are evaluated using a fourth and second order centered scheme respectively, based on a MUSCL finite volume formulation for moving structured meshes. The solution is advanced in time by using an explicit five-step Range–Kutta algorithm. No artificial damping has been added to the numerical schemes. Thus, the centered difference schemes along with a fine mesh, limit numerical dissipation errors as shown in Sect. 6.1.2. The excellent results obtained for free decaying isotropic homogeneous turbulence show that the code is suitable for LES computations (in this case, the subgrid scale model is equivalent to the standard Smagorinsky model [35]). In the rod airfoil configuration, non reflecting boundary conditions and grid stretching in the outer domains are used in order to limit spurious reflections of acoustic waves. For the U-RANS computations, the two-equation Wilcox's $k-\omega$ model [43] is used, where k denotes the turbulent kinetic energy and ω is the specific dissipation rate.

6.1.2 Subgrid scale model

For the LES computations, the eddy viscosity is modeled by using a modified auto-adaptive sub-grid scale (SGS) model. The classical Smagorinsky model [35] expresses the dissipation of the resolved turbulent scales into unresolved ones by an eddy viscosity that is proportional to the square of the filter size and to the square root of $S_{ij}S_{ij}$ where S_{ij} is the strain rate tensor:

$$\nu_{SGS} = C_s^2 \Delta^2 \sqrt{S_{ij}S_{ij}}.$$

C_s is the Smagorinsky constant. The Smagorinsky model is tailored for isotropic homogeneous turbulence and overpredicts the eddy viscosity in strong shear regions where the strain rate increases. In particular, it leads to erroneous results at walls where the SGS viscosity should vanish. A way to improve the wall flow predictions is to multiply the SGS viscosity by the van Driest damping function [40]. This correction is actually adapted to fully developed plane turbulent boundary layers and requires the distance to the wall. However, in complex geometries and in free shear flows, this correction might be wrong or even impossible to apply if the distance to the wall can not be determined. The current auto-adaptative model is also based on a Smagorinsky type approach but the eddy viscosity is not weighted by the van Driest damping function. The strain rate terms are actually weighted in order to reduce the SGS-dissipation in regions of strong shear by a term that reads:

$$3 \times \sqrt{\frac{\frac{1}{\sum_B \bar{S}_{ij}^3}}{\sum_{m,n} \frac{1}{\sum_B \bar{S}_{mn}^3}}},$$

where $\sum_B$ is a sum over the 27 nearest neighbours of the current point. This weighting is actually equivalent to allowing a variation of the Smagorinsky "constant" in non isotropic turbulence. In regions of isotropic homogeneous turbulence, the weighting term is one and thus the classical Smagorinsky model is recovered. The eddy viscosity vanishes at the walls for laminar flows.

Various validation tests have been conducted. For the decay of isotropic homogeneous turbulence, the experimental data of Comte-Bellot et al. [15] at $96d_g$ downstream of the turbulence grid (where d_g is the

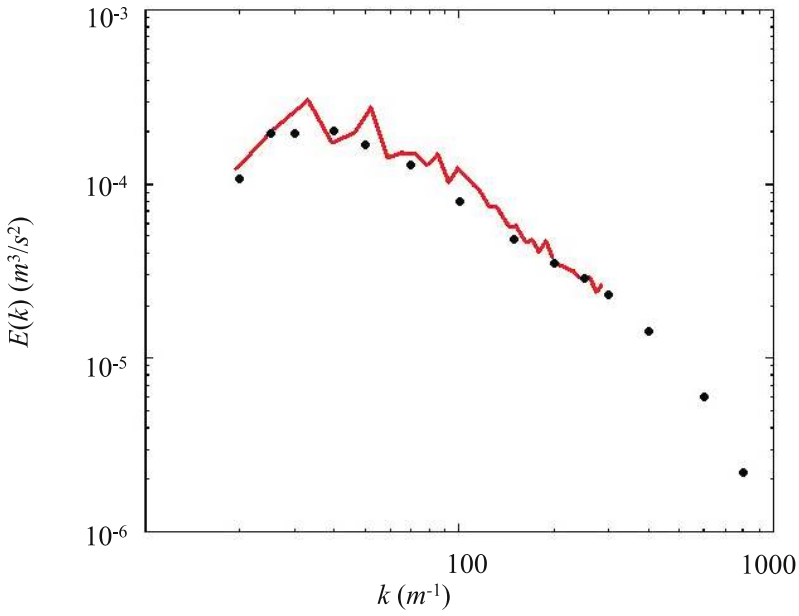

Fig. 13. Decay of isotropic homogeneous turbulence. Comparison of the energy spectra obtained by Comte-Bellot & Corrsin at $96d_g$ downstream of the grid (black dots) and by the LES at time $t = 96d_1/U_\infty$ (red line)

characteristic grid length), operated at a free stream velocity U_∞, are very accurately reproduced by a LES conducted in a periodic box with 33^3 points at an equivalent decay time, $t = 96d_g/U_\infty$, as shown in Fig. 13. This shows that the numerical schemes chosen in the code are suited for LES computations and confirms the fact that the model behaves as the Smagorinsky model in such a flow.

In the case of the channel flow of Moser et al. [30], the LES, that has been carried out agrees very well with the reference DNS as shown in Fig. 14 and the resulting Smagorinsky number follows the van Driest damping function. This channel flow extends over 2δ between the two non slip walls (y direction) and is periodic in the other directions. The Reynolds number based on δ and the friction velocity, is 395. The mesh for the LES contains $50 \times 91 \times 40 = 182\,000$, grid points in the x, y, and z directions, respectively.

For a detailed description and validation of this new SGS model, the reader should refer to Jacob et al. [23]. The advantages of this model are listed below.

- It is easy to implement and to use (no backscattering). In particular it does not require any distance-to-wall information, which is not a relevant parameter in all situations.
- It is cheap to run in comparison to dynamic models. In fact its cost per grid point is of the same order as that of an equivalent RANS computation.
- It applies to the entire flow without any formal restriction.
- Although it is dissipative, the eddy viscosity vanishes for laminar flows. Therefore, a good prediction is expected.

Therefore, it seems suitable for engineering applications. However, since it is only based on heuristic considerations, its universality is not proven on a theoretical basis.

6.1.3 Computational mesh

The inflow conditions and the flow parameters are based on the experimental inflow conditions. However, the jet flow is not modeled in the computation and the angle of attack is zero. The rod-airfoil system is embedded in a uniform flow. The inflow boundary conditions remain the same throughout the computation. The 2D computational mesh for the U-RANS computation is based on 67 000 grid points and is split into seven structured domains. The mesh is refined near solid boundaries ($\Delta y^+ < 8$). Every other grid point of the central part of this mesh is plotted in Fig. 15. The computational time step is about 5×10^{-8} s, corresponding to about 12 000 iterations per aerodynamic cycle. Further details about the computations are given

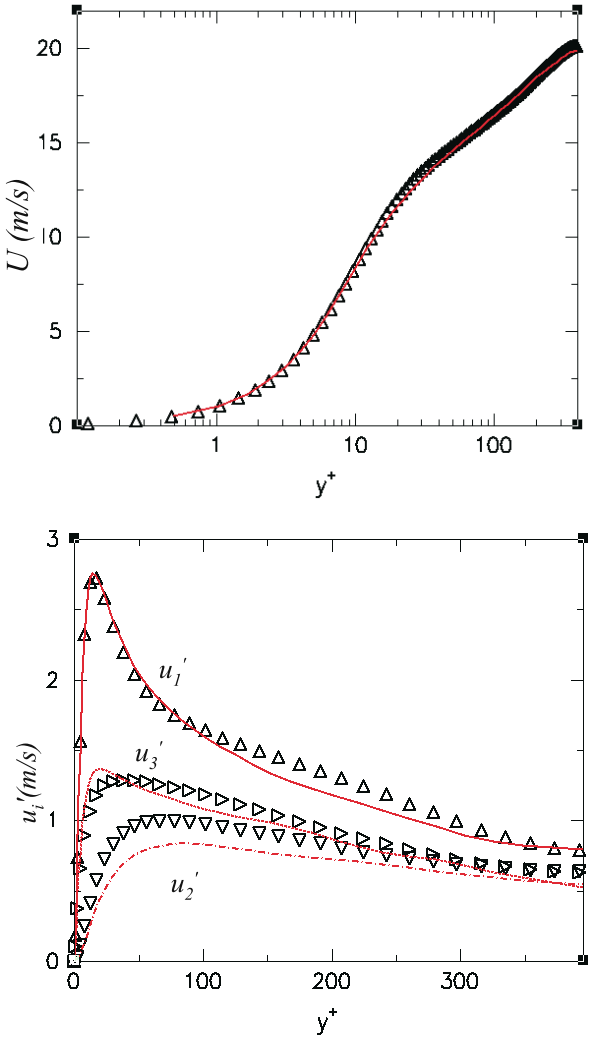

Fig. 14. Channel flow computations: comparison of the present LES (red line) with the DNS Moser et al. (symbols) Top: streamwise mean velocity; bottom: rms values of the velocity fluctuation components. Subscript 1 denotes the mean flow direction, subscript 2, the direction normal to the non-slip walls, subscript 3, the spanwise direction

by Boudet et al. [6]. The 3D computational mesh is based on the 2D mesh, with a higher mesh density near the airfoil walls (353 instead of 253 for the RANS around the airfoil circumference, and 91 instead of 81 points normal to the wall in order to obtain a normal-to-wall mesh size of $\Delta y^+ < 1.3$ and 5.5 on the airfoil and the rod respectively, whereas the mesh size along the airfoil is $\Delta x < 300y^+$ ($\Delta x < 81y^+$ near the leading edge), and the spanwise mesch size is $\Delta z < 350y^+$. The latter values are quite high since they are assumed to scale on the main eddy size. Thus, a very fine mesh is obtained at the leading edge where most of the vortex dynamics occur. The number of grid points at a given spanwise location is about 72 000 and the total mesh size is about 2.2 million, with 31 points in the spanwise direction where the domain extends over $3d$. The mesh density respects the values recommended by Sagaut [33]. The domain is divided into 32 balanced subsets for parallel computations. The time step is about 3×10^{-8} s. A shedding cycle is thus completed in $\sim 20\,000$ iterations and the simulation is run over 10 cycles after convergence to a steady mean flow.

6.1.4 Acoustic predictor scheme

The rotor noise code *Advantia* [12] is used for the acoustic prediction. For the purpose of the present investigation, only surface integrals are computed, since at the current Mach number, the volume sources give a vanishing contribution to the acoustic radiation. The consistency of this approximation has been checked elsewhere [11] by comparing acoustic results obtained from different integration surfaces. For the sake of

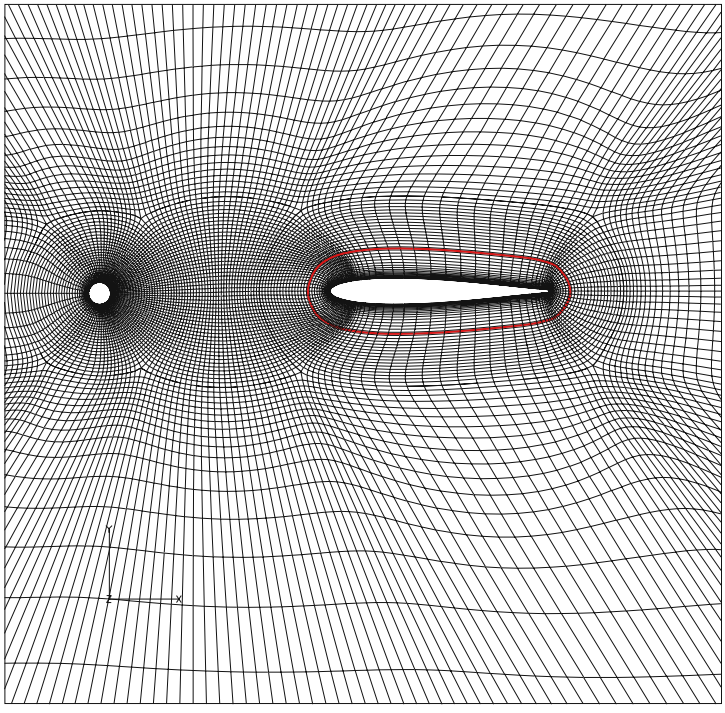

Fig. 15. View of the 2D mesh used for the U-RANS computation along with the integration surface for the sound computation: every other grid point is plotted and the integration surface surrounds the airfoil at distance of $1d$. The LES mesh is denser near the airfoil wall resulting in ~ 5000 additional grid points at each spanwise location

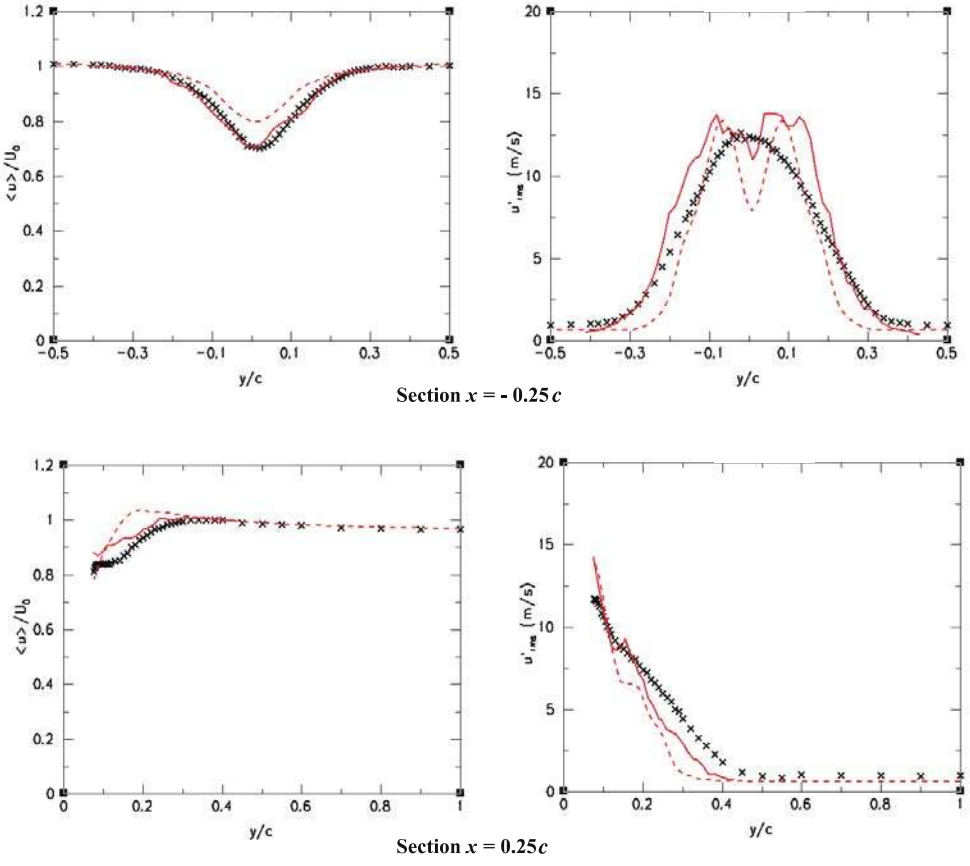

Fig. 16. Example of benchmarking by a comparison of mean flow, u_{rms}. Section [a] (top): $x/c = -0.25$; section [b] (bottom): $x/c = 0.25$; black symbols: experiment; red line: LES; red dashed line: U-RANS

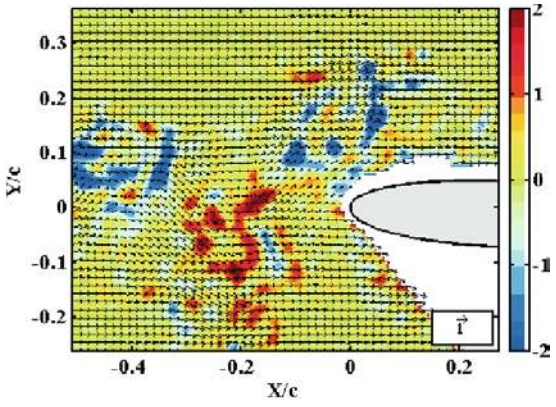

PIV

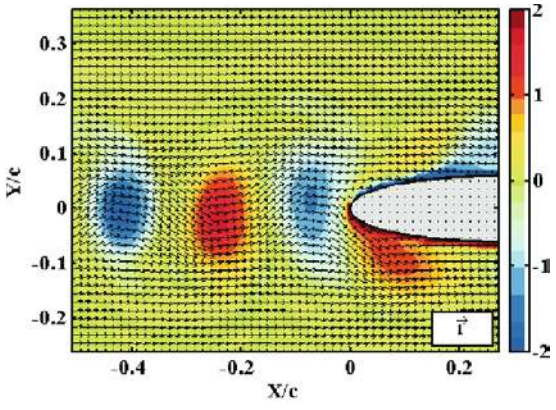

U-RANS

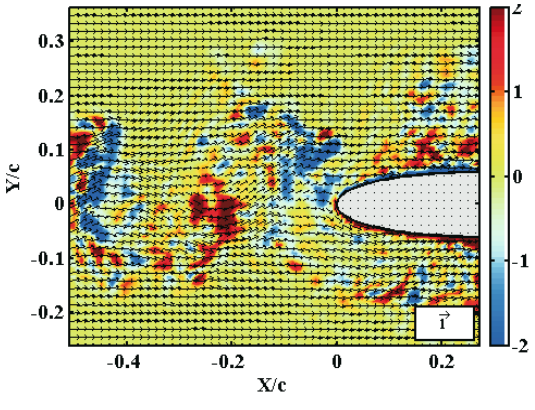

LES

Fig. 17. Example of benchmarking by a comparison of spanwise (z) vorticity snapshots

the present work *Advantia* exploits the retarded time penetrable FW-H formulation proposed by Brentner et al. [9], extended to a moving observer and the advanced-time approach by Casalino et al. [12].

6.1.5 Model for spanwise co–relations

As shown in U-RANS studies for an isolated rod [13] and for the rod-airfoil configuration [11], the spanwise coherence loss of the rod vortex shedding is largely responsible for the broadband part of the far field spectra. Since this coherence loss is not taken into account by U-RANS computations (not even by 3D computations), a stochastic model of the spanwise coherence in the time domain is described in these references.

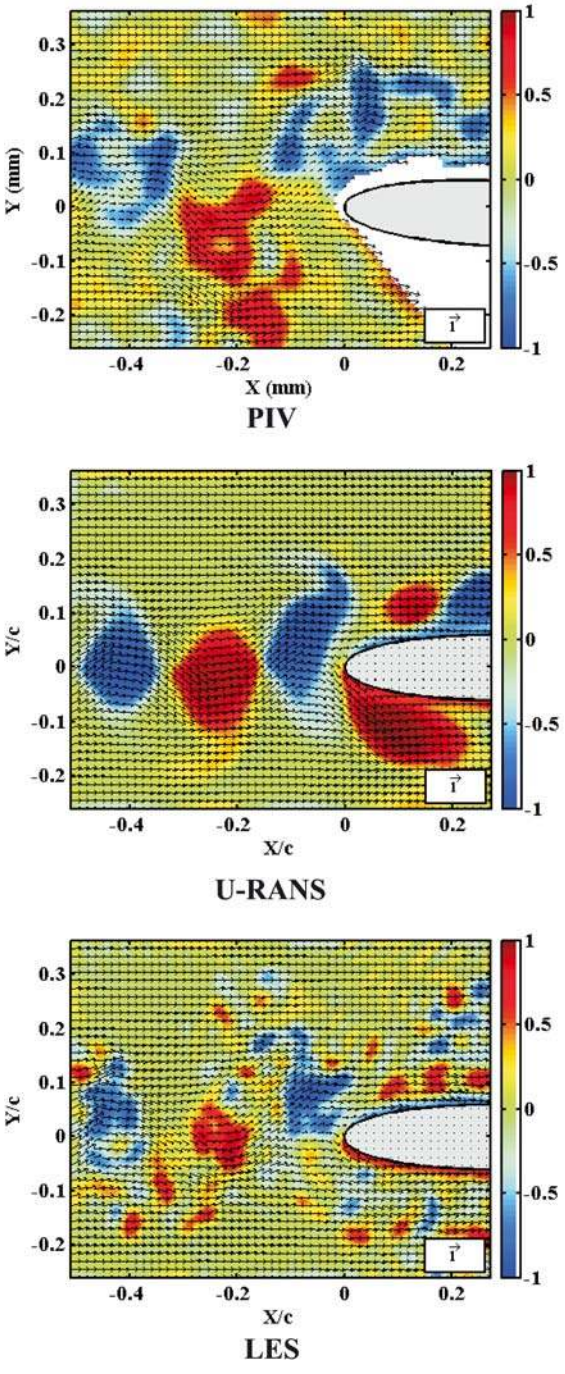

Fig. 18. Example of benchmarking by a comparison of snapshots. Γ_2 function (NAM) applied to PIV (top) and to U-RANS (middle) and LES (bot). The vectors show the relative velocity

The spanwise coherence loss is taken into account by a random Gaussian time shift in the retarded times. The model is discussed and validated in both configurations in ref. [13] and ref. [11]. The validation relies on the present experiment at a lower speed ($M_0 \sim 0.06$) but in the same subcritical Reynolds number range ($Re_d \sim 21\,000$).

6.2 Comparison and validation

In both the U-RANS and the LES computations, the vortex shedding occurs without forcing. The shedding frequency is overestimated by about 25% in the U-RANS computation, the Strouhal number being about

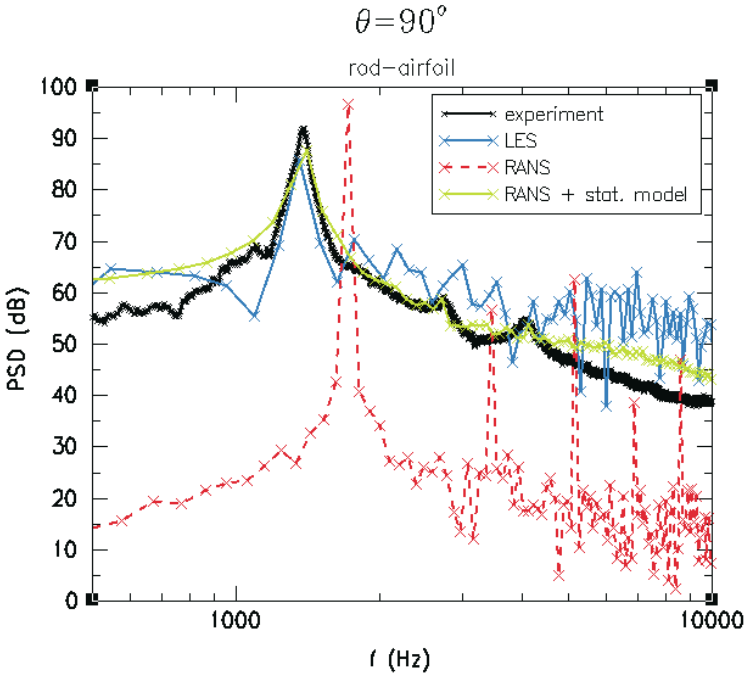

Fig. 19. Example of benchmarking by aa comparison of the acoustic far field at 1.85 m from airfoil center. Experimental: black; LES: blue, U-RANS: red; U-RANS + statistical model: green. The shedding frequency of the green curve has been fitted to the experimental value

0.24. According to literature (see for instance ref. [16] and ref. [24]), this overestimate is typical for 2D computations where turbulent transfers are artificially kept 2D. The vortex dynamics can not be reproduced in a 2D simulation. Actually, a 3D U-RANS computation does not improve this shedding frequency significantly. Indeed, the Strouhal number becomes 0.23, which is still high above the experimental value of 0.19. Moreover the 3D fields appear to be close to a spanwise repetition of the 2D field. The reason for this is due to the role of the 3D spanwise random perturbations that affect the vortex shedding in the real flow. These effects are not described by a U-RANS computation which is intrinsically deterministic. Conversely, the shedding frequency is remarkably well predicted by the LES since the experimental value of 0.19 is found. However, due to the spectral resolution (170 Hz) the accuracy of this prediction is only within 13%. This suggests that the random behaviour of the large, low frequency eddies predicted by an LES, is governing the vortex shedding.

Figures 16, 17, and 18 show some comparisons between the computations and the experiment. The mean flow and *rms* fluctuations that are compared in Fig. 16, show that the U-RANS computation underpredicts turbulent diffusion. The flow gradients are much sharper and the pressure at the leading edge is significantly overpredicted. This is comparable to the well-known overestimate of jet potential cores by U-RANS computations. Again, the LES gives much more accurate results although they are not perfect. This might be due to the fact that the number cycles after convergence (about 10) is too small to carry out proper statistics.

Snapshots of the z-vorticity obtained by PIV, U-RANS and LES are shown in Fig. 17. The number of mesh points for the PIV snapshot is 106 in the x direction and ranges from $x_{\min} = -0.510c$ to $x_{\max} = -0.271c$ whereas it is 85 in the y direction ranging from $y_{\min} = -0.261c$ to $y_{\max} = 0.364c$. The original CFD meshes are finer in this area and are translated onto a cartesian PIV grid for post-processing purposes. The similarity between the experiment and the LES is striking. Differences between these two plots are smaller than the difference between two PIV snapshots (see Sect. 4.2). It is also interesting to observe that the breakdown of the main *von Kármán* vortices into smaller random eddies is well predicted by LES whereas U-RANS only simulates a regular vortex shedding. These plots illustrate in another way the deterministic nature of the U-RANS flow unsteadiness.

An example of instantaneous large scale vortical structures (Γ_2 function) obtained by a NAM analysis from the two computations is compared to the NAM analysis of a PIV snapshot in Fig. 18 for the same snapshot and with the same mesh density as for Fig. 17. The main vortices are quite well predicted even by the U-RANS computation, hence the main flow characteristics are satisfactorily reproduced by the U-

RANS computation. However, these vortices appear much less distorted than in the experiment, which is again a consequence of the deterministic 2D nature, of the flow. The LES plot shows large vortical structures that are even more distorted and split into smaller parts than in the PIV plot. Despite the variety of results shown by the PIV results (Fig. 10, plots (i)–(iv)), this breakdown is never observed on the NAM snapshot proceeded from the experimental data. This may be due to the fact that the co–relation length predicted in the spanwise direction by the LES is smaller (about $4.5d$) than the experimental one (about $6d$). This results in an overestimate of the broadband noise as will be shown in the following.

The acoustic field is computed from the 2D aerodynamic U-RANS fields in two ways.

- The first is a direct application of the Ffowcs–Williams and Hawkings integral to a surface surrounding the airfoil. This computation assumes the field to be fully co-related in the spanwise direction.
- The second approach takes into account the spanwise coherence loss of the vortex shedding. Since the 3D effects are not predicted by the simulation, this is achieved *via* the stochastic model described in Sect. 6.1.3.

In the case of the RANS computation, the spectra can be obtained from a single shedding cycle since the signals are purely periodic. Conversely, the far field computations based on the LES data are carried out by directly applying the Ffowcs–Williams and Hawkings analogy. The spectra are obtained from a discrete fourier transform (DFT) of 18 shedding cycles with 100 points per cycle. The first and last points of the time series are chosen in order to ensure a quasi continuity of the data and thus to avoid spurious broadband components. In order to compare the experimental values (rod and airfoil span $= 30d$) to the LES ones (rod and airfoil span $= 3d$), the CFD far field is integrated along $30d$ by assuming the total field to be the sum of five to ten non co-related fields. This approach assumes the spanwise coherence length to lie within $3d$ and $6d$. Results are shown for the $3d$ case, where the sum is easiest to compute (otherwise an equivalent co-related field has to be extrapolated from the $3d$ data to the coherence length and accounts for an additional 3 dB in the strongest co-related, $6d$ case). Figure 19 shows the comparison of the far field spectra at $\theta = 90°$ obtained from U-RANS by a fully co-related vortex shedding (the integration along the span is performed with a spanwise repetition of the 2D field), a Gaussian co-related shedding (the spanwise statistical model is included in the acoustic analogy), the experimental values, and the far field obtained from the LES. In the case of the statistical modeling, the shedding frequency of the U-RANS spectra has been fitted to the experimental value in order to allow for a better comparison with the experimental spectrum. Since the sound power scales with the square of the frequency, the computed sound level has been reduced by about 2 dB along with the frequency shift.

The fully co-related spectrum is that of a purely periodic signal. This is not surprising since the corresponding (U-RANS) flow field is purely periodic. As a result the peak levels are about 6 dB higher than the experimental values for which the power is spread over a wide frequency range.

In the case of the Gaussian co-related sound computation (from the U-RANS data), a spectral broadening can be observed over a wide range of frequencies. Excellent agreement with experimental values is found for frequencies ranging from the shedding frequency to its second harmonic. At very low as well as at very high frequencies, numerical values are about 5 to 10 dB too high. The level of the main peak is now predicted to be 1.5 dB below the measured value. This surprisingly good agreement shows that the spanwise randomness explains a large part of the broadening around the shedding frequency.

In the case of the far field spectrum computed from the LES data, the shedding frequency is very well predicted (as already mentioned about the flow fields), the spectral broadening extends naturally over a wide range of frequencies and is fairly accurate around the shedding frequency. However, the main peak level is underpredicted by about 7 dB, and a hump of the broadband spectrum occurs in the high frequency range. The former is probably due to the fact that in this Reynolds number range, the unsteady aerodynamic fields are very receptive to the experimental conditions and could explain this discrepancy (as discussed by Boudet et al. [6] for the case of an isolated rod). For the hump, there are various possible explanations. The first is that the LES predicts more small resolved scales than observed in the experiment (as shown by the PIV). Another reason is that the statistics of the LES spectrum are not converged. As an example, the duration of the LES signals is comparable to that required for a single poorly resolved ($\Delta f \sim 170$ Hz) low frequency FFT whereas a statistically reliable computation of the spectrum requires at least 10 or 20 spectra (the present experiment is carried out with 200 averages and $\Delta f = 4$ Hz). The last reason is related to the choice of the integration surface, that is surrounding the airfoil at a distance of one d as shown in Fig. 15. In

this region, the mesh is coarser and could lead to numerical errors in the evaluation of the acoustic sources. In particular, volume sources that are not surrounded by the integration surface might lead to numerical error due to those that cross the integration surface.

This example illustrates how the benchmark can be used to validate a broadband noise model and to evaluate the ability of the CFD technique to predict broadband sources. As has been shown [11], the test case could also be used in order to optimise the choice of the permeable integration surface that is used for the Ffowcs–Williams and Hawkings analogy.

7 Conclusions

The rod-airfoil configuration is shown to be a good benchmark for broadband noise predictions. The present experiment gives information about the main flow statistics, the instantaneous flow structure, and the acoustic field. Future computations should be run with a 2 degree angle of attack and the $y = -2$ mm shift of the rod should not be forgotten, in order to reproduce the experimental conditions as accurately as possible. However, the angle of attack is not believed to have any effect on the leading edge flow, but influences the airfoil wake and the mean pressure around the airfoil.

The spectral broadening around the shedding frequency which occurs at subcritical rod diameter based Reynolds numbers, is convenient for measuring the ability of aeroacoustic models and unsteady CFD solvers to predict broadband noise.

Two examples of benchmarking are shown where a statistical broadband noise model is validated and an acoustic analogy in the time domain as well as a new subgrid scale model are successfully applied to a complex geometry. The comparison of the statistical model against the experiment shows that a large part of the spectral broadening observed in the latter is due to spanwise randomness.

Furthermore, the accuracy of the U-RANS and LES approaches is assessed. U-RANS only predicts deterministic fluctuations of the flow and the corresponding frequencies are inaccurate by 25%. LES provides better predictions of the unsteady flow even of its deterministic part. It gives a realistic estimate of the broadband noise over a large range of frequencies. However, its accuracy is limited by its capability of providing reasonable time samples (required for accurate statistics) at affordable computing costs. This limitation can however be partly overcome by using implicit time advancement.

The experiment also provides interesting physical information about the rod-airfoil configuration. At subcritical Reynolds numbers, the instantaneous flow field is quite different from the classical vortex street picture. Strong 3D effects, secondary vortices, vortex splitting, and stretching significantly distort the flow field and are responsible for spectral broadening around the shedding frequency and its harmonics. They are particularly strong near the leading edge. As a result, the leading edge is the dominant source region. It outranges the rod as a source and the trailing edge which might be responsible for part of the broadband noise.

References

1. Anderson, E., Szewcyk, A.A.: Effects of a splitter plate on the near wake of a circulaire cylinder in 2 and 3-dimensional flow configurations. Exp. Fluids **23**(2), 161–174 (1997)
2. Amiet, R.K.: High freq. thin airfoil theory for subsonic flow. AIAA J. **14**(8), 1076–1082 (1976)
3. Amiet, R.K.: Low freq. approximations in unsteady small perturbation of subsonic flows. J. Fluid Mech. **75**(3), 545–552 (1976)
4. Béra, J.C., Michard, M., Sunyach, M., Comte-Bellot, G.: Changing lift and drag by jet oscillation: experiments on a circular cylinder with turbulent separation. Eur. J. Mech. (Part B/Fluids) **19**, 575–595 (2000)
5. Boudet, J., Casalino, D., Jacob, M.C., Ferrand, P.: Unsteady RANS computations of the flow past an airfoil in the wake of a rod. ASME Paper FEDSM 2002-31343, ASME forum on unsteady flows, Montreal, Canada, July, 14–18 (2002)
6. Boudet, J., Casalino, D., Jacob, M.C., Ferrand, P.: Prediction of sound radiated by a rod using large eddy simulation. AIAA Paper 2003–3217, 9th AIAA/CEAS Aeroacoustics Conf. Hilton Head Island, USA May, 12–14 (2003)
7. Boudet, J., Grosjean, N., Jacob, M.C.: Wake-airfoil interaction as a source of broadband noise. Euromech449 Colloq. Computational Aeroacoustics. Chamonix, France, Dec., 9–12 (2003)
8. Boudet, J., Casalino, D., Jacob, M.C., Ferrand, P.: Prediction of broadband noise: airfoil in the wake of a rod. AIAA Paper 2004–0852, 42nd AIAA Aerospace Conf. Meeting and Exhibit. Reno, USA, Jan., 5–8 (2004)
9. Brentner, K.S., Farassat, F.: Analytical comparison of acoustic analogy and Kirchhoff formulation for moving surfaces. AIAA J. **36**(8), 1379–1386 (1998)

10. Cambanis, V.P., Stapountzis, H.: An experimental study and FLUENT simulation of the horizontal axis wind turbine (HAWT) blade-tower dynamic interaction. 2nd Southeastern Europe Fluent Users Group Meeting. November 1–2, Bucharest, Romania (2001)
11. Casalino, D., Jacob, M.C., Roger, M.: Prediction of rod-airfoil interaction noise using the Ffowcs–Williams and Hawkings analogy. AIAA J. **41**(2), 182–191 (2003)
12. Casalino, D.: An advanced time approach for acoustic analogy predictions. J. Sound Vib. **261**(4), 583–612 (2003)
13. Casalino, D., Jacob, M.C.: Prediction of aerodynamic sound from circular rods via spanwise statistical modeling. J. Sound Vib. **262**(4), 815–844 (2003)
14. Cicala, P.: Le azioni aerodinamiche sul profilo oscillante. L'aerotecnica **16**, 652–665 (1936)
15. Comte-Bellot, G., Corrsin, S.: The use of contraction to improve isotropy of grid-generated turbulence. J. Fluid Mech. **25**(4), 657–682 (1966)
16. Cox, J.S., Rumsey, C.L., Brentner, K.S., Younis, B.A.: Computation of sound generated by viscous flow over a circular cylinder. NASA Tech. Memo. 110339 (1997)
17. Crighton, D.G., Dowling, A.P., Ffowcs-Williams, J.E., Heckl, J.E., Leppington, F.G.: *Modern methods in analytical acoustics*. Springer, London (1992)
18. Filotas, L.T.: Oblique compressible sears function. AIAA J. **12**(11), 1601–1603 (1974)
19. Glauert, H.: *The force and moment on an oscillating airfoil*. British A.R.C., R. & M., No. 1242 (1929)
20. Goldstein, M.E., Atassi, H.M.: A complete second order theory for the unsteady flow about an airfoil due to a periodic gust. J. Fluid Mech. **74**(4), 741–765 (1976)
21. Graftieaux, L., Michard, M., Grosjean, N.: Combining PIV, POD, and vortex identification algorithms for study of unsteady turbulent swirling flows. Meas. Sci. Tech. **11**, 1422–1429 (2001)
22. Graham, J.W.S.: Similarity rules for thin airfoils in non-stationary subsonic flows. J. Fluid Mech. **43**(4), 753–766 (1970)
23. Jacob, M.C., Boudet, J., Casalino, D., Caro, J., Grosjean, N., Michard, M.: A feasibility study on the use of CFD to model broadband noise generation. *Final report, deliverable D1.15, E.U. Project TurboNoise CFD, contract No. G4RD-CT-1999-00144*, (2003)
24. Kato, C., Ikegawa, M.: Large eddy simulation of the unsteady wake of a circular cylinder using the finite element method. Adv. in numerical simulation of turbulent flows. **117**, 49–56 (1991)
25. Küssner, H.G.: Zusammenfassender Bericht über den instationären Auftrieb von Flügeln. Luftfahrtforschung **13**, 410–424 (1936)
26. Magagnato, F., Sorgüven, E., Gabi M.: Far field noise prediction by large-eddy simulation and Ffowcs–Williams and Hawkings analogy. AIAA paper 2003-3206, 9th AIAA/CEAS Aeroacoustics Conf., Hilton Head Island, May 12–14 (2003)
27. Martinez, R., Widnall S.: Unified aerodynamic-acoustic theory for a thin rectangular wing encountering a gust. J. Sound Vib. **41**(4), 407–420 (1980)
28. Michard, M., Graftieaux, L., Lollini, L., Grosjean, N.: Identification of vortical structures by a non local criterion: application to PIV measurements and DNS-LES results of turbulent rotating flows. 11th Symp. on turbulent shear flows, Grenoble, France (1997)
29. Michard, M., Jacob, M.C., Grosjean, N.: An experimental charaterization of the flow past an airfoil in the wake of a circular rod. ASME FEDSM Paper 2002-31344, ASME forum on unsteady flows, Montreal, Canada, July, 14–18 (2002)
30. Moser, R.D., Kim, J., Mansour, N.N.: Direct numerical simulation of turbulent channel flow up to $Re_\tau = 590$. Phys. Fluids, Brief communications **11**(4), 943–945 (1999)
31. Pérènnes, S., Roger, M.: Aerodynamic noise of a two-dimensional wing with high-lift devices. AIAA Paper 98-2338, Proc. 4th AIAA/CEAS Aeroacoustics Conf., 772–782, Toulouse, France 2–4 June, (1998)
32. Possio, C.: L'azione aerodynamica sul profilo oscillante in un fluido compressibile a velocitá iposonora. L'Aerotecnica **18**(4), 441–458 (1938)
33. Sagaut, P.: *Introduction à la simulation des grandes échelles pour les écoulements de fluide incompressible (revised and augmented version)*. Mathématiques et Applications, Springer (2002)
34. Sears, W.R.: Some aspects of non-stationary airfoil theory and its practical application, J. Aeronaut. Sci. **8**(3), 104–108 (1941)
35. Smagorinsky, J.: Numerical study of small-scale intermittency in three-dimensional turbulence. Month. Weather Rev. **91**, 99–164 (1963)
36. Sorgüven, E., Magagnato, F., Gabi M.: Acoustic prediction of a cylinder and airfoil configuration at high Reynolds numbers with LES and FWH. ERCOFTAC Bullentin **58**, 47–50 (2003)
37. Stapountzis, H., Yakinthos, K., Goulas, A., Kallergis, L.S., Kambanis, V.: Cylinder wake airfoil interaction with application to downwind HAWT. Proc. Eur. Wind Energy Conf., E.L. Petersen (Ed.), James & James, 172–175 (1999)
38. Strouhal, V.: Über eine besondere Art der Tonerregung. Ann. Phys. Chem. **3**(5), 216–251 (1878)
39. Unal, M.F., Rockwell, D.: On the vortex formation of a cylinder. Part 2: control by a splitter plate interference. J. Fluid Mech. **90**, 513–529 (1987)
40. van Driest, E.R.: On the turbulent flow near a wall. J. Aeronaut. Sci. **23**, 1007–1011 (1956)
41. Wagner, H.: Über die Enstehung des dynamischen Auftriebes von Tragflügeln. ZAMM **5**(1), 17–35 (1925)
42. Widnall, S.: Helicopter noise due to blade-vortex interaction. J. Acous. Soc. Am. **51**(1), 345–365 (1971)
43. Wilcox, D.C.: Comparison of two equation turbulence models for boundary layers with pressure gradients, AIAA J. **31**, 1414–1421 (1993)
44. Zdravkovich, M.M.: *Flow around circular cylinders, vol. 1: fundamentals*. Oxford Sci. Pub., Oxford uni. Press. (1997)